



저작자표시-비영리-변경금지 2.0 대한민국

이용자는 아래의 조건을 따르는 경우에 한하여 자유롭게

- 이 저작물을 복제, 배포, 전송, 전시, 공연 및 방송할 수 있습니다.

다음과 같은 조건을 따라야 합니다:



저작자표시. 귀하는 원저작자를 표시하여야 합니다.



비영리. 귀하는 이 저작물을 영리 목적으로 이용할 수 없습니다.



변경금지. 귀하는 이 저작물을 개작, 변형 또는 가공할 수 없습니다.

- 귀하는, 이 저작물의 재이용이나 배포의 경우, 이 저작물에 적용된 이용허락조건을 명확하게 나타내어야 합니다.
- 저작권자로부터 별도의 허가를 받으면 이러한 조건들은 적용되지 않습니다.

저작권법에 따른 이용자의 권리는 위의 내용에 의하여 영향을 받지 않습니다.

이것은 [이용허락규약\(Legal Code\)](#)을 이해하기 쉽게 요약한 것입니다.

[Disclaimer](#)

理學碩士 學位論文

**Computational studies on the photophysical
properties of organic TADF molecules and the
stability of supramolecular complex**

(열활성지연형광 유기분자의 광물리 성질과
초분자 복합체의 안정성에 대한 전산화학연구)

蔚山大學校大學院
化學科
吳智勳

**Computational studies on the photophysical
properties of organic TADF molecules and the
stability of supramolecular complex**

(열활성지연형광 유기분자의 광물리 성질과
초분자 복합체의 안정성에 대한 전산화학연구)

指導教授 정재훈

이 論文을 理學碩士學位 論文으로 제출함
2018年 11月

蔚山大學校大學院

化學科

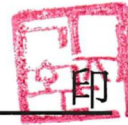
吳智勳

吳智勳의 理學碩士 學位 論文을 認准함

審査委員 이 민 형



審査委員 지 기 환



審査委員 정 재 훈



蔚山大學校大學院

2018年 11月

Abstract

Density functional theory (DFT) method is known to be a powerful method for calculating not only the energy at the exact ground state, but also the various factors that determine the properties of the molecule. In addition, the phenomenon involving the excited state, such as electronic transition can be dealt with using time-dependent density functional theory (TD-DFT) method. In this paper, we have studied on TADF, which have recently in limelight as the luminescent principle of next-generation light-emitting diodes (OLEDs) using DFT and TD-DFT methods. In particular, on the second main topic, studies on supramolecular systems have been successful in explaining the experimental results by using the DFT method strategically. The following text gives you more insight into the useful and varied uses of computational chemistry.

Contents

I. Introduction

I.1. Organic light-emitting diodes (OLEDs).....	7
I.1.1. Evolution of OLEDs.....	7
I.1.2. Thermally-activated delayed fluorescence (TADF).....	9
I.2. Supramolecular chemistry	11

II. Methodological background..... 13

II.1. Hohenberg-Kohn theorem.....	13
II.2. Kohn-Sham equation.....	13
II.3. Exchange-correlation energy.....	17
II.4. Time-dependent density functional theory (TD-DFT).....	17

III. Results and Discussion..... 20

III.1. Properties of organic TADF molecules	
III.1.1. Specific TADF molecular design	20
III.1.2. Color tuning for the organic TADF molecules	31
III.2. Effect of the non-covalent interaction on the supramolecular formation	
III.2.1. Molecular Borromean rings (BRs)	47

IV. Conclusion..... 56

V. Reference..... 58

List of tables

Chapter III.

Table 2.1. Photophysical data of *ortho*-carbazole-appended triarylboron compounds in toluene.

Table 2.2. The contribution (in %) of donor and acceptor moieties to the frontier molecular orbitals and overlap integrals ($I_{H/L}$) between them for *ortho*-carbazole-appended triarylboron compounds (1–5).

Table 2.3. The calculated absorption wavelength (λ_{abs} , in nm) and the corresponding oscillator strength (f) for *ortho*-carbazole-appended triarylboron compounds (1–5).

Table 2.4. The calculated emission wavelength (λ_{abs} , in nm) and the corresponding oscillator strength (f) for *ortho*-carbazole-appended triarylboron compounds (1–5).

List of Figures

Chapter I.

Figure 1.1. Illustration of general idea of OLEDs.

Figure 1.2. Illustration of light generation of OLEDs.

Figure 1.3. Reported examples of various supramolecular systems.

Chapter II.

Figure 1.3. Schematics of a typical DFT procedure by self-consistent field loop.

Chapter III.

Figure 1.1. The optimized dihedral angle ($^{\circ}$) between donor and phenylene (top) and frontier molecular orbitals, HOMO and LUMO, of *ortho*-D–A compounds (isovalue = 0.03) at their ground state (S_0) geometries from DFT calculations. The orbital energy, HOMO–LUMO gap (E_g), energy splitting between S_1 and T_1 states (ΔE_{ST}), and overlap integral extent ($I_{H/L}$) are presented.

Figure 1.2. The optimized dihedral angle ($^{\circ}$) between donor and phenylene (top) and frontier molecular orbitals, HOMO and LUMO, of *para*-D–A compounds (isovalue = 0.03) at their ground state (S_0) geometries from DFT calculations. The orbital energy, HOMO–LUMO gap (E_g), energy splitting between S_1 and T_1 states (ΔE_{ST}), and overlap integral extent ($I_{H/L}$) are presented.

Figure 1.3. Transient PL decay curves of (a) DPA o B and CzoB and (b) DPA p B and Cz p B in oxygen-free toluene at 298 K. The inset shows the temperature dependence of transient PL decays.

Figure 1.4. Transient PL decay curves of the host films doped with (a) **PXZoB** (6 wt%), (b) **DPAoB** (30 wt%), and (c) **CzoB** (20 wt%) at 298 K.

Figure 1.5. UV/Vis absorption (left) and PL spectra (right) of PXZoB, DPAoB, and CzoB in toluene (5.0×10^{-5} M) at room temperature.

Figure 2.1. (a) UV/vis absorption and (b) PL spectra of **1–5** in toluene (2.0×10^{-5} M) at room temperature.

Figure 2.2. Cyclic voltammograms of **1–5** (1.0×10^{-3} M in MeCN except for the reduction of **5** (DMF), scan rate = 100 mV s⁻¹ for oxidation and 200 mV s⁻¹ for reduction).

Figure 2.3. Transient PL decay curve of **2** in oxygen-free toluene at 298 K. The inset shows the temperature dependence of transient PL decay.

Figure 2.4. Transient PL decay curves of *ortho* D–A compounds in oxygen-free toluene at 298 K. Inset: temperature dependence of decay in oxygen-free toluene.

Figure 2.5. Optimized dihedral angles (θ , in degrees) between donor and phenylene (top) and frontier molecular orbitals, HOMO and LUMO, of **1–5** (isovalue = 0.03) at their ground state (S_0) geometries from DFT calculations (PCM in toluene). The orbital energies, HOMO–LUMO gaps (E_g), energy splitting between the S_1 and T_1 states (ΔE_{ST}), and overlap integral extents ($I_{H/L}$) are presented.

Scheme 3.1. Self-assembly and interconversion of Borromean rings and monomeric rectangles.

Figure 3.1. Reported examples of Borromean rings (a) Metal associated Borromean rings (b) Real Borromean rings after demetallation (c) Real Borromean rings wearing paramagnetic Cu(I) ions

Figure 3.2. X-ray crystal structures of (a) **1** \supset (2·pyrene), (b) **3** , (c) **2s** and (d) **4**. Hydrogen atoms and counter anions are omitted for clarity.

Figure 3.3. Crystal structure of Borromean rings **2** (a) in space filling model (b) Length and breadth of the ring in Borromean rings topology (one of the rings has been deleted for clarity).

Figure 3.4. Crystal structure of Borromean rings **2** in ball-stick model showing (a) $\pi \cdots \pi$ and (b) $\text{CH} \cdots \pi$ interactions responsible for Borromean rings topology (one of the rings has been deleted for clarity).

Figure 3.5. RDG iso-surfaces ($s = 0.5$ au) for BRs **2**. The surfaces are colored on a blue–green–red scale according to the values of $\text{sign}(\lambda_2)\rho$, ranging from -0.02 to $+0.02$ au. The primary intermolecular interactions are the π - π interactions between phenyl-ethynyl-pyridinyl moieties of donor **L**₁ and tetracene moieties of the acceptor **A**, which are indicated by green iso-surfaces.

Chapter I. Introduction

I.1. Organic light-emitting diodes (OLEDs)

I.1.1. Evolution of OLEDs

Display technology has been evolving for thinner, lighter, higher resolution, and better energy efficiency, such as cathode ray tube (CRT), plasma display panel (PDP), and liquid-crystal display (LCD). Organic light-emitting diodes (OLEDs) display, which have remarkable development over a period of about 30 years with the observation of organic-electroluminescence (EL) from anthracene single crystals in 1963, is the most advanced technology.¹ In addition, it is currently used in mobile displays, televisions, and electronics display panel, which are commonly found around us. In particular, OLEDs display have a variety of advantages, such as very fast response times of thousands or tens of thousands times, unlimited viewing angles and high purity colors, unlike previous generation LCDs. Despite these great advantages, however, it still inferior in terms of price competitiveness. The luminescent of OLEDs has been mainly focused on mechanisms using fluorescence and phosphorescence. However, fluorescence has disadvantages of low quantum efficiency because it uses only singlet excitons. In case of phosphorescence, intersystem crossing (ISC) by spin-orbit coupling is necessary, therefore, heavy metal is required. Hence, it has disadvantages in terms of toxicity and cost.

Device Structure

Cathode
Electron Injection Layer (EIL)
Electron Transport Layer (ETL)
Emission Layer (EML)
Hole Transport Layer (HTL)
Hole injection Layer (HIL)
Anode

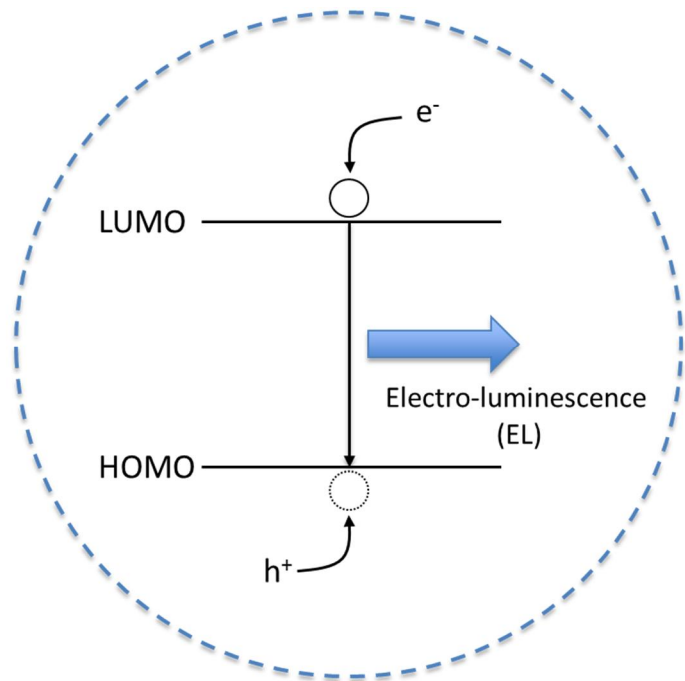


Figure 1.1. Illustration of general idea of OLEDs

I.1.2. Thermally-activated delayed fluorescence (TADF)

Thermally-activated delayed fluorescence (TADF) is in limelight as a next-generation technology in organic light-emitting diodes (OLEDs) luminescent principle because it can achieve theoretically 100% quantum efficiency while compensating for the disadvantages of fluorescence and phosphorescence.

TADF materials have been attracting a significant interest as emitters in OLEDs that exhibit high efficiency, comparable to that of OLEDs with phosphorescent emitters, but without needing to use costly heavy metals.²⁻⁹ The high efficiency in TADF-OLEDs is realized by up-conversion of triplet excitons into emissive singlet excitons via the thermally activated reverse intersystem crossing (RISC) process.^{5, 8-16} Because fast RISC is a key feature required to attain highly efficient TADF, TADF emitters usually need to exhibit very small energy splitting (ΔE_{ST}) between the excited singlet (S_1) and triplet (T_1) states. Construction of TADF emitters with a twisted donor (D)–acceptor (A) structure has been widely adopted to effectively reduce the spatial overlap between the highest occupied molecular orbitals (HOMO) and lowest unoccupied molecular orbitals (LUMO), which thereby reduces ΔE_{ST} .⁹ Accordingly, D–A compounds consisting of sterically hindered donor and/or acceptor groups have been extensively studied as molecular scaffolds for TADF emitters.

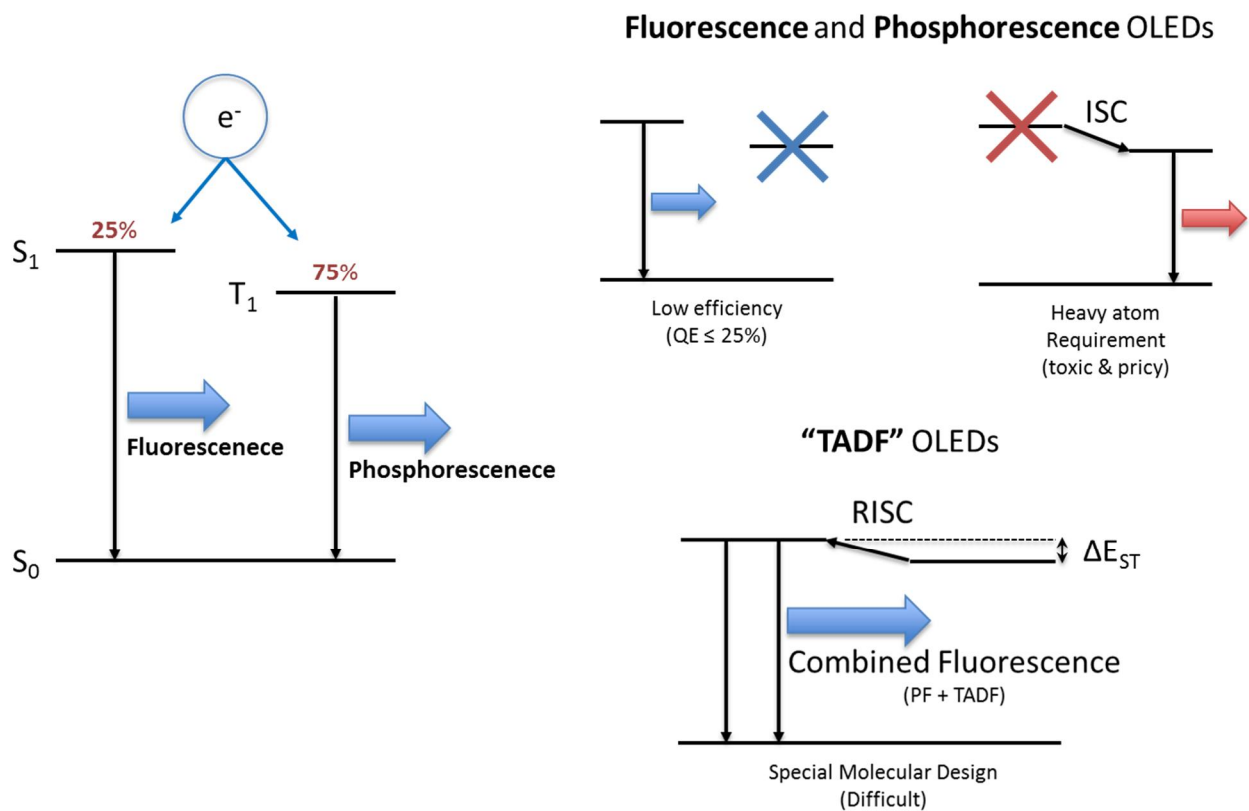


Figure 1.2. Illustration of light generation of OLEDs

I.2. Supramolecular chemistry

Supramolecular chemistry is the domain of chemistry beyond that of molecules that focuses on the chemical systems made up of a discrete number of assembled molecular subunits or components. The forces responsible for the spatial organization may vary from weak (intermolecular forces, electrostatic or hydrogen bonding) to strong (covalent bonding), provided that the degree of electronic coupling between the molecular component remains small with respect to relevant energy parameters of the component. While traditional chemistry focuses on the covalent bond, supramolecular chemistry examines the weaker and reversible noncovalent interactions between molecules. These forces include hydrogen bonding, metal coordination, hydrophobic forces, van der Waals forces, pi-pi interactions and electrostatic effects. The study of non-covalent interactions is crucial to understanding many biological processes from cell structure to vision that rely on these forces for structure and function. Biological systems are often the inspiration for supramolecular research.

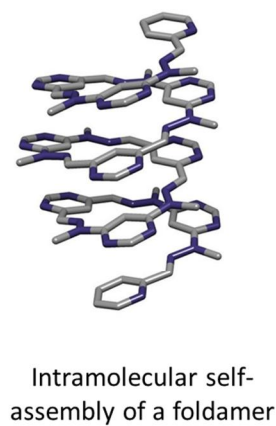
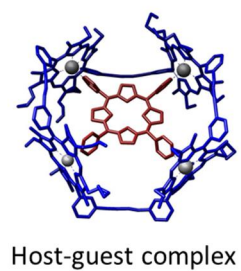
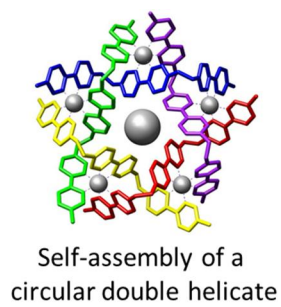
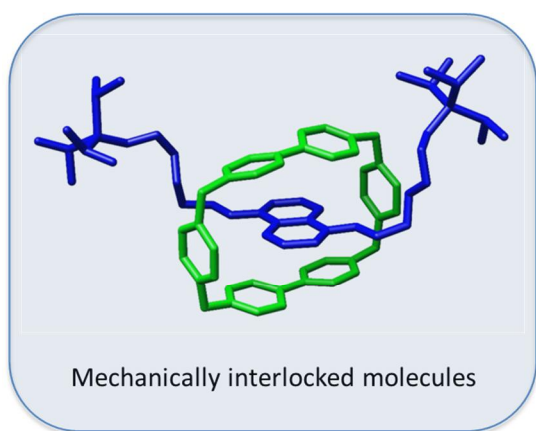


Figure 1.3. Reported examples of various supramolecular systems.

Chapter 2. Methodological background¹⁷⁻²⁰

II.1. Hohenberg-Kohn theorem

Following the Born-Oppenheimer fixed nuclei approximation came two pivotal theorems in the history of density functional theory (DFT) posited by Hohenberg and Kohn¹⁷. In the first theorem, they said that for any system of interacting particles in an external potential, $V_{ext}(\mathbf{r})$, i.e. a potential external to the electrons, there is a unique (apart from an additive constant) ground state particle density, $\rho_0(\mathbf{r})$. And secondly, that for any external potential, $V_{ext}(\mathbf{r})$, it is possible to define the total energy, E as a functional of the density, i.e. $E[\rho(\mathbf{r})]$. Furthermore, for any $V_{ext}(\mathbf{r})$, the ground state density, $\rho_0(\mathbf{r})$ is found at the global minimum of $E[\rho(\mathbf{r})]$.

II.2. Kohn-Sham equation

The Kohn–Sham equation is the one electron Schrödinger equation of a fictitious system of non-interacting particles that generate the same density as any given system of interacting particles. This equation is defined by a local effective external potential in which the non-interacting particles move, typically denoted as $V_{eff}(\mathbf{r})$ or $V_s(\mathbf{r})$.

The Kohn-Sham equation is as follows,

$$H_i^{KS} \psi_i(\mathbf{r}) = E_i \psi_i(\mathbf{r}) \text{ for each 1-electron } i$$

$$H_i^{KS} = \left[-\frac{1}{2} \nabla_i^2 - \sum_k \frac{Z_k}{|r_{ik}|} + \frac{1}{2} \iint \frac{\rho(\mathbf{r}')}{|\mathbf{r}_i - \mathbf{r}'|} d\mathbf{r}' + V_{xc}(\rho) \right]$$

1st term ; Kinetic energy of electron i

2nd term ; $V_{ext}(\rho)$ for electron i and nucleus k

3rd term ; V_H for electron i and $\rho(\mathbf{r}')$

4th term ; exchange-correlation potential of electron i

$$\left[-\frac{1}{2} \nabla_i^2 + V_{eff}(\rho) \right] \psi_i(\mathbf{r}) = E_i \psi_i(\mathbf{r})$$

$$V_{eff}(\rho) = V_{ext}(\rho) + V_H(\rho) + V_{xc}(\rho) : \text{Kohn-Sham effective potential}$$

This Kohn-Sham equation is similar to Hartree-Fock equation, but it has some different things. Firstly, the exchange-correlation energy term, $V_{xc}(\rho)$ is added, and secondly, the potential terms become a density function that depends on electron density.

The energy of each potential terms in the Kohn-Sham hamiltonian is as follows,

$$E_{kin}(\psi_i) = -\frac{1}{2} \int \psi^*(r) \nabla_i^2 \psi(r) dr$$

$$E_{ext}(\rho) = - \int \frac{Z_k}{|r_{ik}|} \rho(r) dr$$

$$E_H(\rho) = \frac{1}{2} \iint \frac{\rho(r)\rho(r')}{|r_i - r'|} dr dr'$$

$$E_{xc}(\rho) = \int \varepsilon_{xc}[\rho(r), \Delta\rho(r)] dr \text{ for LDA and GGA}$$

$\varepsilon_{xc}(\rho) \equiv$ exchange-correlation energy per volume of constant ρ

\equiv simple function of ρ with parameters

$$\equiv \frac{1}{2} \int \frac{\rho_{xc}(r, r')}{|r - r'|} dr'$$

The Kohn-Sham energy of the system focusing on electrons (except for atomic nucleus energy) is as follows,

$$E_{total} = E_{KS} = E_{kin}(\psi_i) + E_{ext}(\rho) + E_H(\rho) + E_{xc}(\rho)$$

and a solving process of the Kohn-Sham equation is given as below,

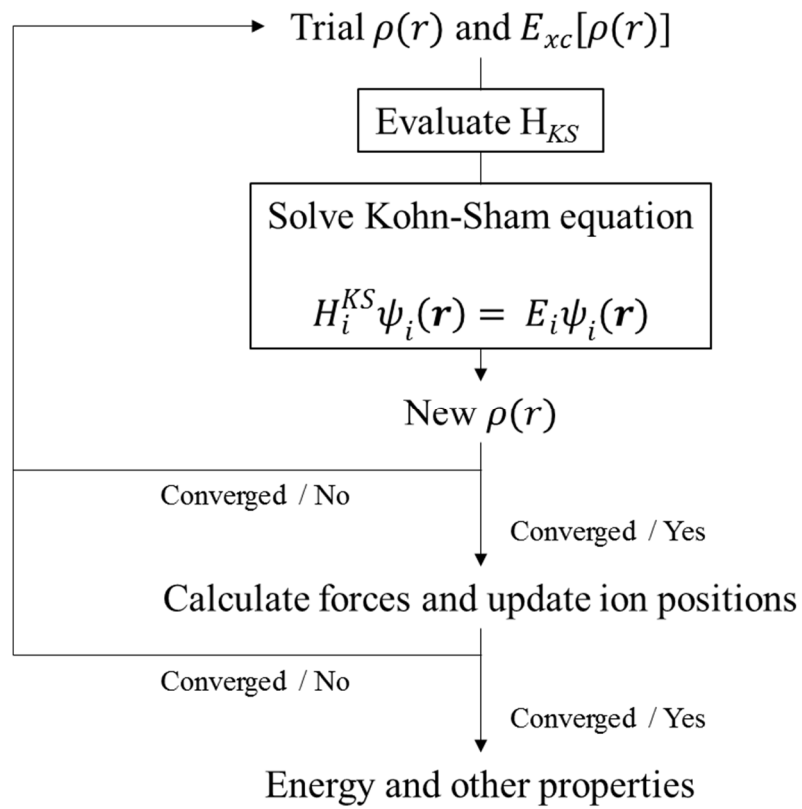


Figure 1.3. Schematics of a typical DFT procedure by self-consistent field loop.

II.3. Exchange-correlation energy

Kohn and Sham calculate all the potentials and energies with the electron density function, and approximate the quantum mechanical exchange-correlation energy that is excluded in calculations. Accordingly, the total potential in DFT model is the Kohn-Sham effective potential, $V_{eff}(\mathbf{r})$ based on this model. However, the electron density and their energy are same as in n-electrons system, in practically. The portion of the exchange-correlation energy in the total energy is about 10% or more lower than, but this energy is determine the fundamental properties of materials, such as the formation and dissociation of bonds, bandgap, spin interaction and so on. Thus, the important thing is depend on that how we precisely approximate for the exchange-correlation energy, i.e. $E_{xc}(\rho)$.

II.4. Time-dependent density functional theory (TD-DFT)

DFT can yield excellent ground state properties, such as structural parameters, formation and dissociation energies and so on. However, DFT is a ground state theory and can not, in principle, yield excited state properties, electronic dynamics, or in general to study time-dependent problems. Therefore, we have to use the time-dependent density functional theory (TD-DFT) method to solve various problems that are tied to time dependency.

The evolution of the wavefunction is governed by

$$\hat{H}(t)\Psi(t) = [\hat{T} + \hat{V}_{ee} + \hat{V}_{ext}]\Psi(t) = i\frac{d\Psi(t)}{dt}, \quad \text{for a given } \Psi(0)$$

where

$$\hat{T} = -\frac{1}{2}\sum_{i=1}^N v_{ext}(\mathbf{r}_i, t)$$

$v_{ext}(\mathbf{r}, t)$ contains an explicit time-dependence (e.g., a laser field) or an implicit time-dependence (e.g., the nuclei are moving).

The time-dependent electronic density is

$$n(\mathbf{r}, t) = N \int d^3 r_2 \cdots \int d^3 r_N |\Psi(\mathbf{r}, \mathbf{r}_2, \dots, \mathbf{r}_N, t)|^2$$

The Runge-Gross theorem proves a one-to-one correspondence between the density and the external potential

$$n(\mathbf{r}, t) \leftrightarrow v_{ext}(\mathbf{r}, t)$$

The theorem states that the densities $n(\mathbf{r}, t)$ and $n'(\mathbf{r}, t)$ evolving from a common initial state $\Psi(t=0)$ under the influence of two potentials $v_{ext}(\mathbf{r}, t)$ and $v'_{ext}(\mathbf{r}, t)$ eventually differ if the potentials differ by more than a purely time-dependent function:

$$\Delta v_{ext}(\mathbf{r}, t) = v_{ext}(\mathbf{r}, t) - v'_{ext}(\mathbf{r}, t) \neq c(t) .$$

We define a fictitious system of noninteracting electrons that satisfy time-dependent Kohn-Sham equations:

$$i \frac{\partial \psi_j(\mathbf{r}, t)}{\partial t} = \left[-\frac{\nabla^2}{2} + v_{KS}[n](\mathbf{r}, t) \right] \psi_j(\mathbf{r}, t),$$

whose density,

$$n(\mathbf{r}, t) = \sum_{j=1}^N |\psi_j(\mathbf{r}, t)|^2,$$

is defined to be precisely that of the real system. By virtue of the one-to-one correspondence proven in the previous section, the potential $v_{KS}(\mathbf{r}, t)$ yielding this density is unique.

We then define the exchange-correlation potential via:

$$v_{KS}(\mathbf{r}, t) = v_{ext}(\mathbf{r}, t) + v_H(\mathbf{r}, t) + v_{xc}(\mathbf{r}, t)$$

where the Hartree potential has the usual form,

$$v_H(\mathbf{r}, t) = \int d^3 r' \frac{n(\mathbf{r}', t)}{|\mathbf{r} - \mathbf{r}'|},$$

The exchange-correlation potential is a functional of the entire history of the density, $n(\mathbf{r}, t)$, the initial interacting wavefunction $\Psi(0)$, and the initial Kohn-Sham wavefunction, $\psi(0)$. This functional is a very complex one, much more so than the ground-state case. Knowledge of it implies solution of all time-dependent Coulomb interacting problems.

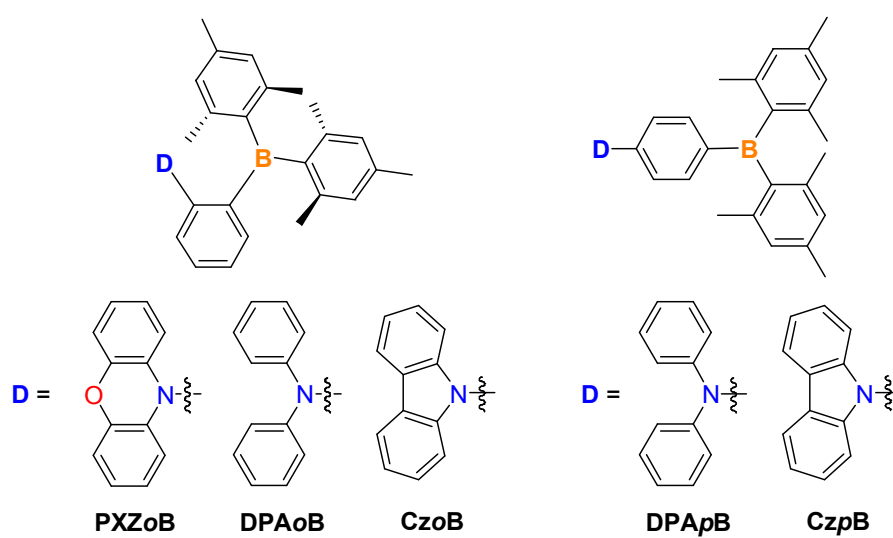
Chapter III. Results and Discussion

III.1. Properties of organic based TADF molecules

III.1.1. Specific TADF molecular design

Generally, TADF molecules having a donor-acceptor structure are composed of a multiple donor type having two or more donors in one acceptor, a dual core type having two donors and acceptors in a molecule, and spacer system incorporating phenyl spacer.²¹ In this study, we have investigated TADF molecules are composed of phenoxazine (PXZ), diphenylamine (DPA), and carbazole (Cz) donor and dimesityl borane (BMes₂) acceptor based on a spacer system (Chart 1.1). Furthermore, we performed a computation studies to investigate their geometric, electronic, and photophysical properties.

Chart 1.1. Chemical structures of *ortho*- and *para*-donor-appended triarylboron compounds



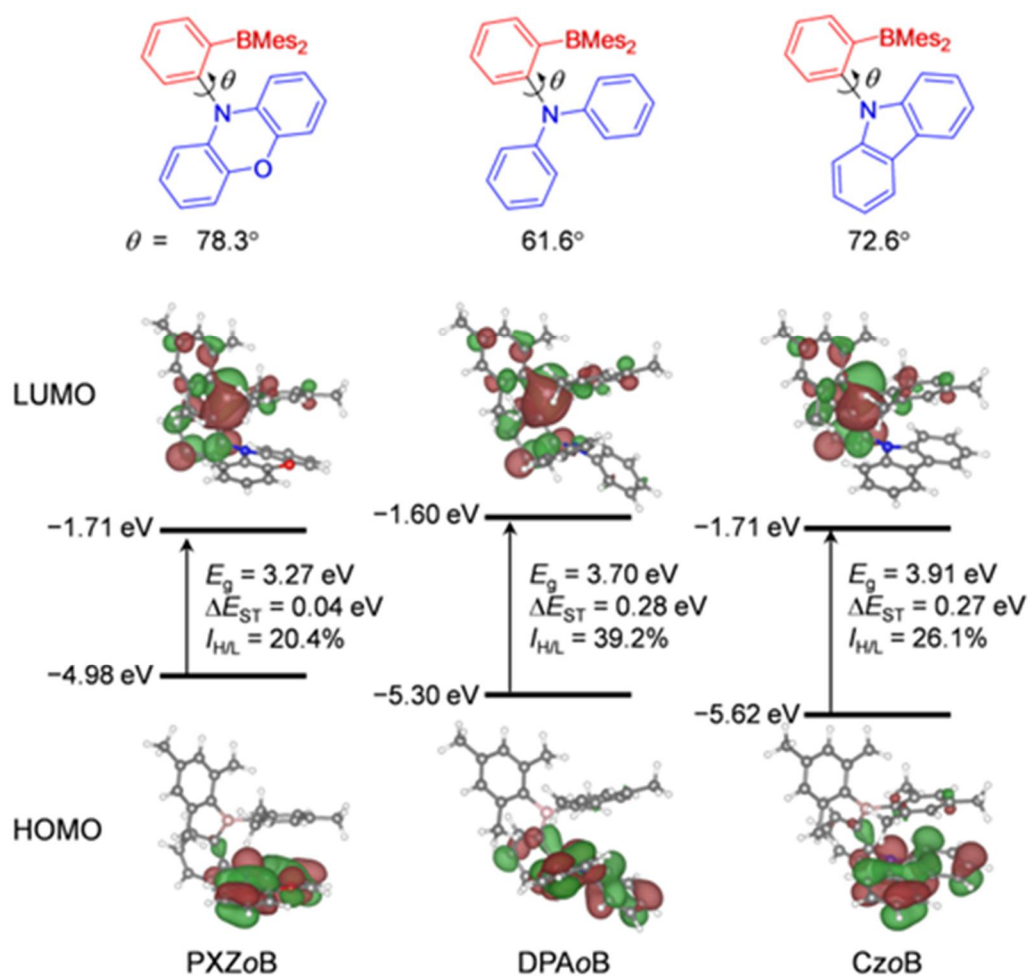


Figure 1.1. The optimized dihedral angle ($^\circ$) between donor and phenylene (top) and frontier molecular orbitals, HOMO and LUMO, of *ortho*-D–A compounds (isovalue = 0.03) at their ground state (S_0) geometries from DFT calculations. The orbital energy, HOMO–LUMO gap (E_g), energy splitting between S_1 and T_1 states (ΔE_{ST}), and overlap integral extent (I_{HL}) are presented.

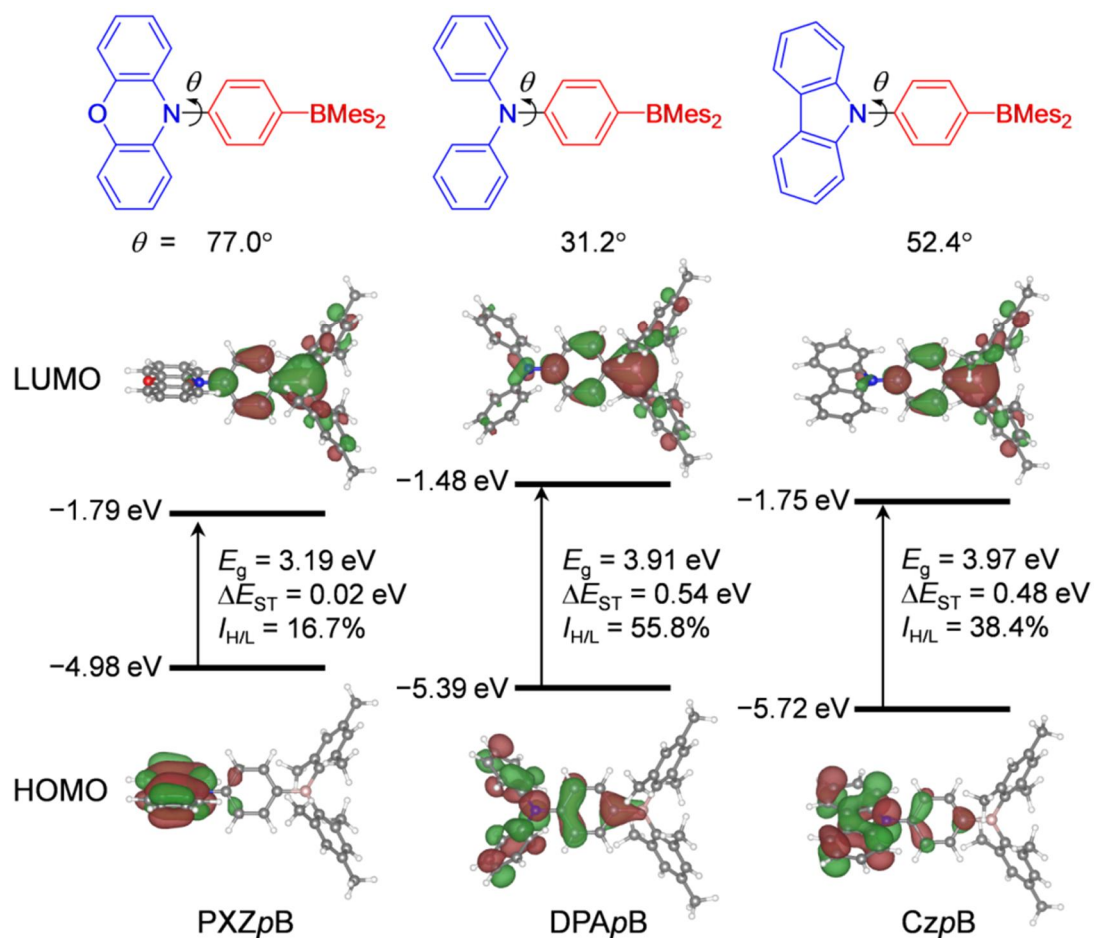


Figure 1.2. The optimized dihedral angle ($^\circ$) between donor and phenylene (top) and frontier molecular orbitals, HOMO and LUMO, of *para*-D–A compounds (isovalue = 0.03) at their ground state (S_0) geometries from DFT calculations. The orbital energy, HOMO–LUMO gap (E_g), energy splitting between S_1 and T_1 states (ΔE_{ST}), and overlap integral extent ($I_{H/L}$) are presented.

Table 1.1. The contribution (in %) of donor and acceptor moieties to the frontier molecular orbitals for the *ortho*-D–A compounds, **PXZoB**, **DPAoB**, and **CzoB**, and their *para* derivatives, **PXZpB**, **DPApB**, and **CzpB**.

	MO	Energy (eV)	donor	acceptor (phenylene)	acceptor (BMes ₂)
PXZoB	LUMO	-1.71	1.99	34.01	64.00
	HOMO	-4.98	94.80	3.23	1.97
DPAoB	LUMO	-1.60	4.45	30.64	64.91
	HOMO	-5.30	78.88	17.58	3.54
CzoB	LUMO	-1.71	2.13	34.26	63.61
	HOMO	-5.62	89.34	5.39	5.27
PXZpB	LUMO	-1.79	1.75	35.73	62.52
	HOMO	-4.98	96.71	3.15	0.14
DPApB	LUMO	-1.48	8.31	32.69	59.00
	HOMO	-5.39	66.25	28.02	5.73
CzpB	LUMO	-1.75	3.77	33.13	63.10
	HOMO	-5.72	84.42	13.01	2.57

Table 1.2. The calculated absorption wavelength (λ_{abs} , in nm) and the corresponding oscillator strength (f) for the *ortho*-D–A compounds, **PXZoB**, **DPAoB**, and **CzoB**, and their *para* derivatives, **PXZpB**, **DPApB**, and **CzpB**.

	λ_{abs}	f_{abs}
PXZoB	517.5	0.0035
DPAoB	439.6	0.0762
CzoB	408.4	0.0073
PXZpB	497.6	0.0287
DPApB	385.3	0.7449
CzpB	377.2	0.4029

TADF properties of the ortho- and para-D-A compounds are as follows. TADF was similarly observed in the transient PL decay curves of the doped host film of the *ortho*-D-A compounds (Figure 1.4). In sharp contrast, the *para*-D-A compounds, DPA_pB and Cz_pB, only displayed single-exponential PL decay profiles with similar short-lived lifetimes (~ ns) for both the oxygen-free and aerated solutions (Figures 1.3 and Table 1.3). This result clearly demonstrates the normal fluorescent nature of DPA_pB and Cz_pB. As the analogous *para*-PXZ derivatives of PXZ_oB were reported to show strong TADF,^{22, 23} the TADF property of the present PXZ_oB could be reasonably understood. However, for the D-A compounds with DPA and Cz donors, the unique TADF for the *ortho*-derivatives is remarkable because the *para*-derivatives do not display delayed fluorescence. This structural difference led to different ΔE_{ST} values in toluene. Experimentally, the ΔE_{ST} values were 0.20 and 0.15 eV for DPA_oB and Cz_oB, respectively, which were small enough for efficient TADF. However, DPA_pB and Cz_pB showed large ΔE_{ST} values of 0.41 and 0.39 eV.

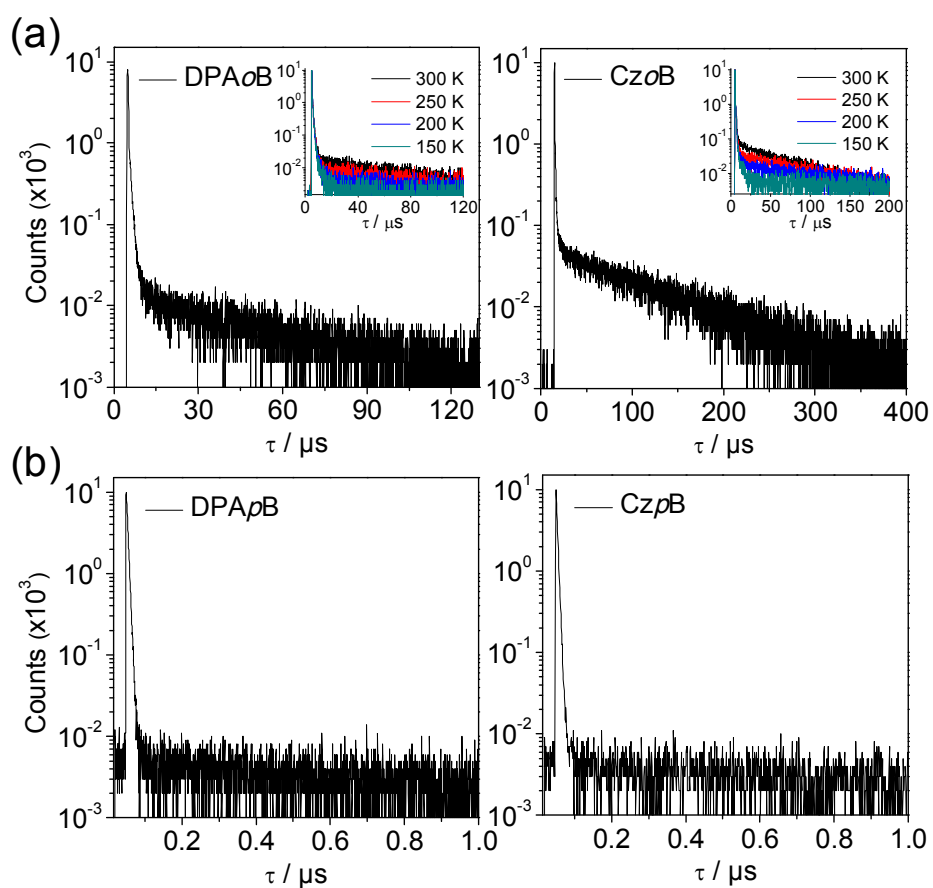


Figure 1.3. Transient PL decay curves of (a) DPAoB and CzOB and (b) DPApB and CzpB in oxygen-free toluene at 298 K. The inset shows the temperature dependence of transient PL decays.

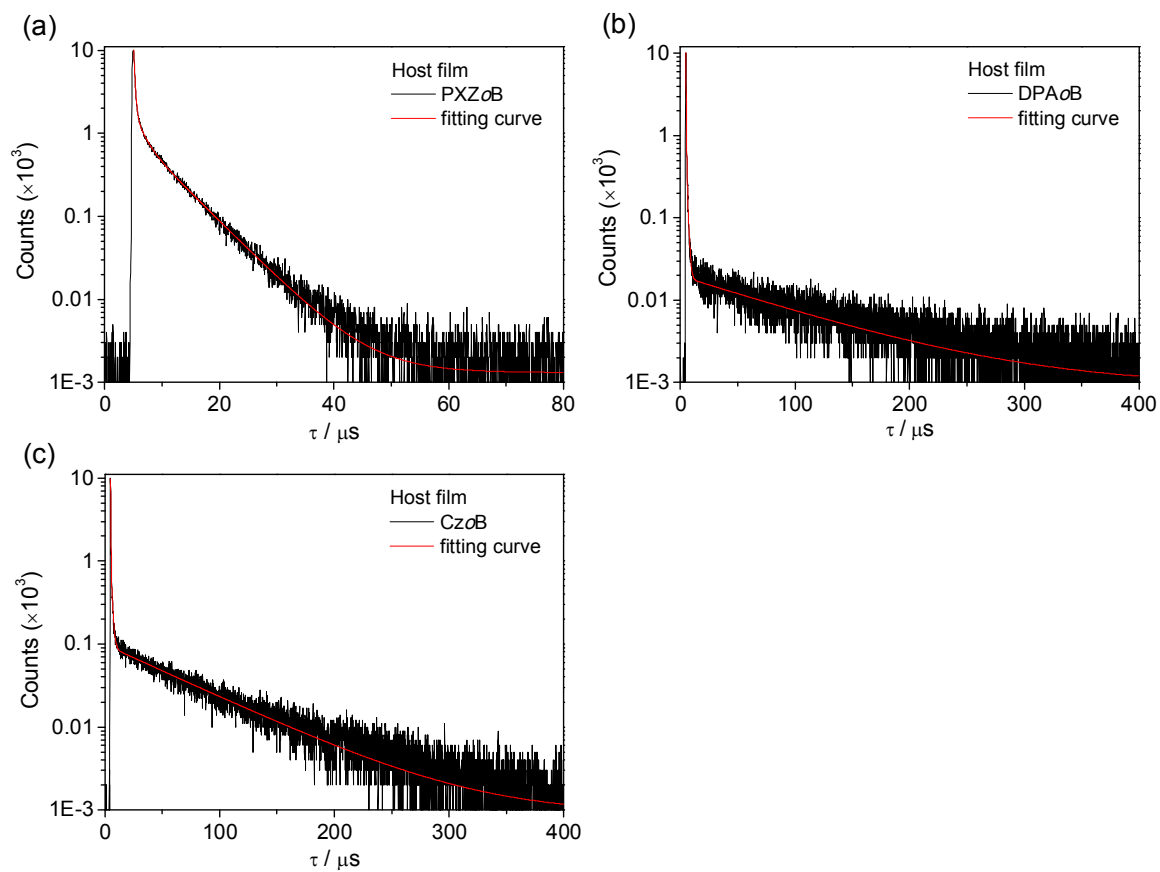


Figure 1.4. Transient PL decay curves of the host films doped with (a) **PXZoB** (6 wt%), (b) **DPAoB** (30 wt%), and (c) **CzoB** (20 wt%) at 298 K.

To gain further insight into the geometric, electronic, and optical properties of the *ortho*-D–A compounds and their *para* derivatives, we performed a computational study based on DFT. The geometries of ground (S_0) and excited (S_1 and T_1) states were fully optimized with the DFT and time-dependent DFT (TD-DFT) methods, respectively (Figures 1.1 and 1.2). The optimized dihedral angles between the donor and acceptor moieties at the ground states for DPA o B (61.6°) and CzoB (72.6°) were much larger than those of their *para* derivatives, DPA p B (31.2°) and Cz p B (52.4°), indicating steric congestion in the *ortho*-compounds. For PXZ o B, the dihedral angle of 78.3° is similar to that of PXZ p B (77.0°). Note that the computed angles for PXZ o B and CzoB are comparable to those observed in the crystal structures (79.0° and 76.6°). The HOMOs of PXZ o B and PXZ p B are exclusively distributed to the donor PXZ moiety at 94.8 and 96.7%, respectively, due to their large dihedral angles (Table 1.1). In contrast, DPA o B and CzoB led to the effective spatial separation of HOMO and LUMO distributions, whereas their *para* derivatives with smaller dihedral angles exhibited co-distribution in the central phenylene ring. The effective spatial separation of HOMO and LUMO is of importance in determining ΔE_{ST} , as ΔE_{ST} is closely related to the overlap integral ($I_{H/L}$) between the wavefunctions for HOMO and LUMO.^{24, 25} Moderate $I_{H/L}$ values were obtained in three *ortho*-D–A compounds (20.4% for PXZ o B, 39.2% for DPA o B, and 26.1% for CzoB), indicating good separation of HOMO and LUMO.²⁶ Importantly, the calculated ΔE_{ST} values were small for *ortho*-D–A compounds ($\Delta E_{ST} = 0.04\text{--}0.28$ eV),

but substantial ΔE_{ST} and $I_{H/L}$ values were obtained for the corresponding *para*-compounds, DPA*p*B and CzpB; ΔE_{ST} of 0.54 eV and $I_{H/L}$ of 55.8% for DPA*p*B, 0.48 eV and 38.4% for CzpB. The lowest-energy absorption and emission processes for *ortho*-D–A compounds were characterized as a HOMO–LUMO transition, i.e., ICT in nature (Table 1.2). The calculated transition energies are also in good qualitative agreement with their experimental wavelengths showing a gradual increase in the energy following the order of PXZ*o*B < DPA*o*B < CzoB (Table 1.3 and Figure 1.5).

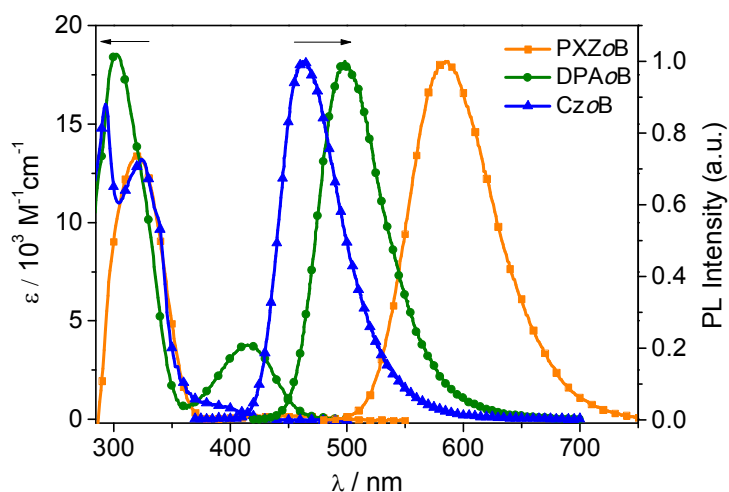


Figure 1.5. UV/Vis absorption (left) and PL spectra (right) of PXZO, DPAO, and CZO in toluene (5.0×10^{-5} M) at room temperature.

Table 1.3. Photophysical Data of *Ortho*- and *Para*-D–A Compounds in Toluene

compd	λ_{abs}^a (nm)	λ_{PL}^a (nm)	Φ_{PL}^b (%) (N ₂ /air)	τ_p^c (Φ_{PF}) (ns (%))	τ_d^c (Φ_{DF}) (μs (%))	HOMO/LUMO ^d (eV)	E_S/E_T^e (eV)	ΔE_{ST}^f (eV) (exp./calc.)
PXZO	320, 445	585	23/6	62 (8)	2.92 (15)	-5.07/-2.35	2.44/2.44	<0.01/0.04
DPAO	302, 415	498	73/38	27 (42)	14.4 (31)	-5.33/-2.41	2.76/2.56	0.20/0.28
CZO	324, 380	463	79/19	38 (24)	71.6 (55)	-5.55/-2.32	2.95/2.80	0.15/0.27
DPApB	309, 380	437	91/80	4.0 (91)	<i>g</i>	<i>h</i>	3.12/2.71	0.41/0.54
CZpB	291, 360	401	75/65	3.7 (75)	<i>g</i>	<i>h</i>	3.33/2.94	0.39/0.48

^aIn oxygen-free toluene at 298 K (5.0×10^{-5} M). ^bAbsolute photoluminescence quantum yields (PLQYs) in oxygen-free (N₂) and air-saturated (air) toluene at 298 K. ^cPL lifetimes of prompt (τ_p) and delayed (τ_d) decay components for the oxygen-free toluene solutions at 298 K. The estimated prompt (Φ_{PF}) and delayed (Φ_{DF}) portions (%) in transient decay curves are given in parentheses. ^dEstimated from the electrochemical oxidation (HOMO) and reduction (LUMO). ^eSinglet (E_S) and triplet (E_T) energies estimated from onset wavelengths of the fluorescence and phosphorescence spectra obtained at 77 K. ^f $\Delta E_{\text{ST}} = E_S - E_T$. Calculated ΔE_{ST} from TD-DFT at PBE0/6-31G(d,p). ^gNot observed. ^hNot measured.

III.1.2. Color tuning for the organic TADF molecules

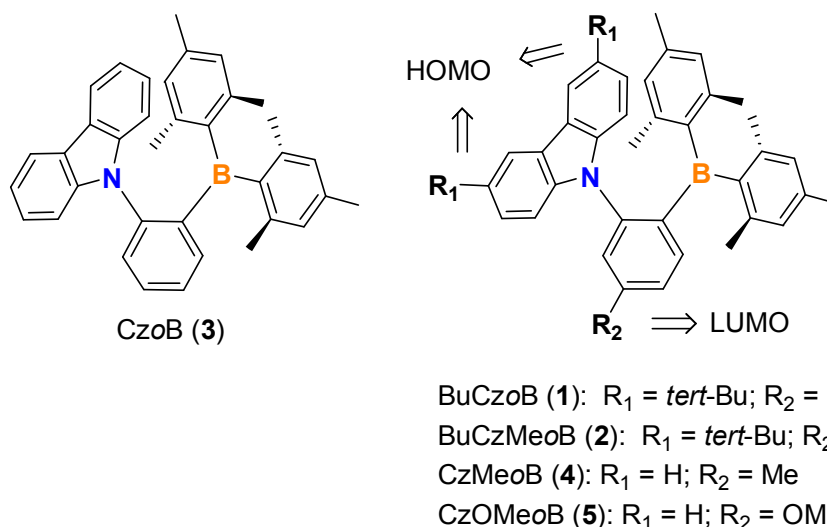
As we saw in the previous section, efficient TADF emitters have to satisfy a small energy splitting between the singlet and excited triplet states, i.e. ΔE_{ST} . Also, it was revealed that geometrical characters are important, such as twisted D-A structure, in order to obtain small ΔE_{ST} . In this section, we will introduce a study of color tuning via band gap control based on a CzoB scaffold that showed good TADF properties.

As a new approach to a twisted D–A structure, we recently reported *ortho*-donor-appended triarylboron compounds as highly efficient TADF emitters (e.g., CzoB in Chart 2.1).²⁷ Owing to the *ortho* D–A connectivity²⁸⁻³⁰ and bulky nature of the triarylboron acceptor,³¹⁻³⁵ these compounds were sterically "locked" and showed a highly twisted arrangement between the donor and acceptor moieties. In addition, the triarylboron acceptor possesses strong electron-accepting properties due to its empty $p_{\pi}(B)$ orbital, which can exert a strong LUMO localization effect.³⁶⁻³⁸ Consequently, in sharp contrast to the normal fluorescence of their *para* derivatives, the *ortho* compounds displayed strong TADF in both solution and film states.²⁷ The resulting OLED devices incorporating an *ortho*-carbazole-appended triarylboron emitter (CzoB, **3**) showed pure blue emission along with a very high external quantum efficiency (EQE) of 24.1%. This finding was regarded as particularly promising for the development of efficient blue OLEDs, for which the device performance still lags behind those of green and red OLEDs,^{11, 39-45} albeit a very recent report by Cheng et al. demonstrated pure blue

OLEDs with a record-high EQE over 31%.⁴⁶ It is also important to note that the twisted D–A structure does not tend to easily undergo structural relaxation, which can cause broadening and red-shifting of the blue emission profile.^{3,37} Since CzoB compound may constitute a prototype of blue *ortho* D–A TADF emitters, we envisage that further enhancement in the device performance and tuning of the emission color over the entire blue region can be systematically achieved by manipulating the electronic structure of molecules, such as the HOMO and LUMO. This could be readily accomplished by introducing substituents into the donor and/or acceptor moieties while retaining their rigid backbone structure.

To this end, we prepared a series of D–A emitters based on a CzoB scaffold, in which various electron-donating groups, such as *tert*-Bu, Me, and OMe, are introduced to the carbazole donor and/or to the phenylene ring of the dimesitylphenylboron (PhBMes₂) acceptor (Chart 2.1).

Chart 2.1. *Ortho*-carbazole-appended triarylboron compounds.



To investigate the feasibility of blue emission tuning and the delayed fluorescence properties, the UV/vis absorption and PL spectra were measured in toluene for all of the compounds (Figure 2.1 and Table 4). While the strong absorption in the high-energy region of ca. 300–350 nm can be mainly assigned to local transitions in the donor and acceptor moieties (i.e., the carbazole-centered π – π^* transition⁴⁷⁻⁴⁹ and the triarylboron-centered $\pi(\text{Mes})$ – $p\pi(\text{B})$ charge transfer (CT) transition^{2, 50-52}), the broad low-energy absorptions centered at ca. 370–410 nm can be ascribed to the intramolecular charge transfer (ICT) transition between the donor and acceptor moieties. Although weak in intensity, the ICT band undergoes gradual shifts in the wavelength depending on the substituents of the carbazole and phenylene rings (inset in Figure 2.1.a); while

introduction of a *tert*-Bu group on the carbazole leads to a bathochromic shift by elevating the HOMO level, the Me and OMe groups on the phenylene ring increase the LUMO level, resulting in hypsochromic shifts. Consequently, *tert*-Bu-substituted **1** exhibits absorption at the lowest energy region, whereas OMe-substituted **5** shows the most blue-shifted absorption among the compounds.

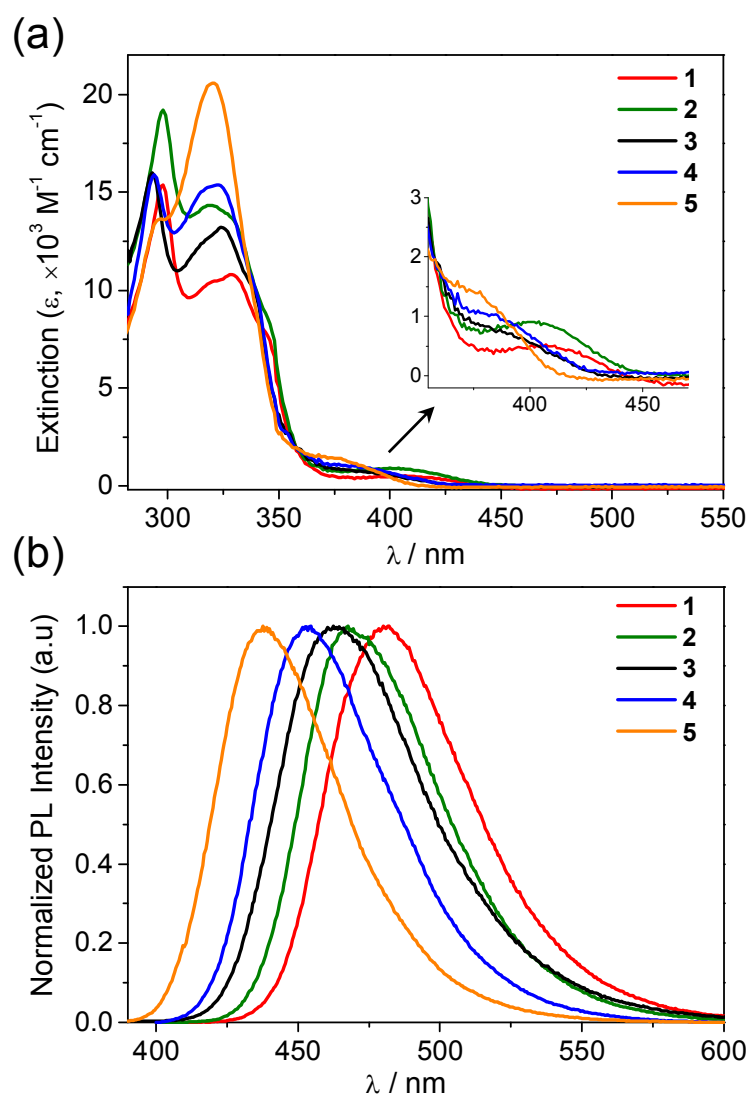


Figure 2.1. (a) UV/vis absorption and (b) PL spectra of **1–5** in toluene (2.0×10^{-5} M) at room temperature.

This band gap control, accomplished by adjusting the HOMO and LUMO levels, is consistent with the electrochemical data (Figure 2.2 and Table 2.1). Attaching *tert*-Bu groups to the carbazole slightly reduces the oxidation potential by ca. 0.07 V (raising the HOMO level) compared to those of the unsubstituted compounds (**1**, **2** vs. **3–5**). Note that the substitution of *tert*-Bu groups at the 3- and 6-positions of carbazole leads to reversible oxidation due to the increased stability of radical cations. Alternatively, all of the compounds undergo boron-centered, reversible reduction, where the potential is negatively shifted (raising the LUMO level), upon substitution of Me and OMe groups at the phenylene moiety relative to the unsubstituted compounds (**2**, **4**, **5** vs. **1**, **3**). Because of the spatial separation of HOMO and LUMO within a molecule, it is likely that the substituent exerts its electronic effect mainly on the respective donor and acceptor moieties. Accordingly, the electrochemical band gap (E_g) can be fine-tuned in the order of **5** > **4** > **3** > **2** > **1**.

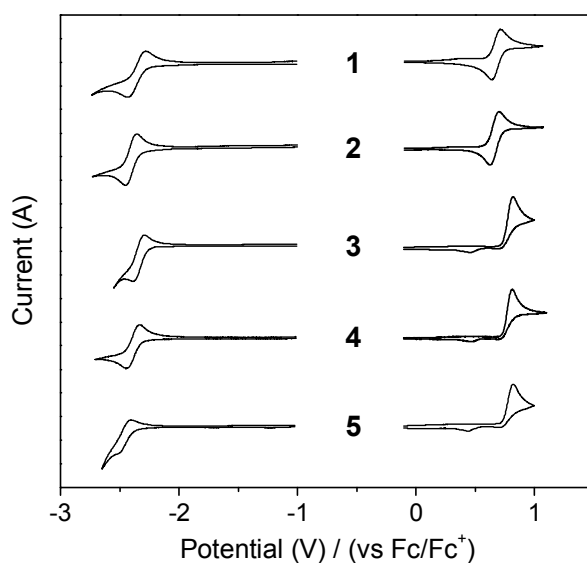


Figure 2.2. Cyclic voltammograms of **1–5** (1.0×10^{-3} M in MeCN except for the reduction of **5** (DMF), scan rate = 100 mV s^{-1} for oxidation and 200 mV s^{-1} for reduction).

The PL spectra for all compounds exhibit structureless, ICT emission bands in the blue region (Figure 2.1.b). The emission bands gradually undergo hypsochromic shifts from sky blue ($\lambda_{\text{PL}} = 481 \text{ nm}$ for **1**) to ultra-deep blue ($\lambda_{\text{PL}} = 438 \text{ nm}$ for **5**) following the band gaps of the compounds. This result demonstrates the facile manipulation of the blue emission by introducing substituents to the donor and/or acceptor moieties in the proposed system. PL quantum yields (PLQY, Φ_{PL}) of the compounds were measured in oxygen-free and air-saturated toluene solutions. The compounds show moderate ($\Phi_{\text{PL}} = 42\%$ for **5**) to very high PLQYs ($\Phi_{\text{PL}} = 92\%$ for **2**) in oxygen-free toluene. *tert*-Bu-substituted **1** and **2** are more emissive than unsubstituted carbazole compounds **3–5**, whose PLQYs decrease with increasing emission energy (Φ_{PL} of **3** > **4** > **5**). The fact

that the PLQYs tend to undergo a significant decrease and are very similar to each other in air-saturated toluene ($\Phi_{\text{PL}} = \text{ca. } 18\text{--}20\%$) suggests that the high PLQYs in oxygen-free toluene can be attributed to the efficient $T_1 \rightarrow S_1$ RISC, the extent of which is greater for **1** and **2** than for **3–5**. The upconversion from the T_1 to S_1 states was further investigated by transient PL decay measurements (Figure 2.3 and 2.4). All of the compounds feature strong delayed fluorescence in oxygen-free toluene, as noted by the microsecond-range delayed (τ_d) components of the PL decay curves at 298 K. Furthermore, the temperature dependence of PL decay confirms that the delayed fluorescence is assignable to TADF.⁹ When compared to the similar level of the prompt portions (Φ_{PF}), the delayed portion (Φ_{DF}) of the transient decay curve is in the order of $\mathbf{1} \approx \mathbf{2} > \mathbf{3} > \mathbf{4} > \mathbf{5}$, implying that the difference in the PLQYs of the compounds mainly originates from the different contributions of delayed fluorescence. We attribute this primarily to the different ΔE_{ST} values among the compounds. In fact, the experimentally determined ΔE_{ST} values of **1** and **2** ($\Delta E_{\text{ST}} < 0.1$ eV) are smaller than those of **3–5** ($\Delta E_{\text{ST}} = 0.15\text{--}0.16$ eV) although all of the ΔE_{ST} values are sufficiently small for efficient TADF. As previously noted in the parent CzoB (**3**),²⁷ these results indicate that the substituted *ortho* D–A compounds in this study can act as strong TADF emitters due to the inherent *ortho* connectivity between their bulky donor and acceptor moieties.

Table 2.1. Photophysical data of *ortho*-carbazole-appended triarylboron compounds in toluene.

Compd	λ_{abs} [nm] ^{a)}	λ_{PL} [nm] ^{a)}	Φ_{PL} [%] (N ₂ /air) ^{b)}	τ_{p} (Φ_{PF}) [ns] [%] ^{c)}	τ_{d} (Φ_{DF}) [μ s] [%] ^{c)}	HOMO/LUMO [eV] ^{d)}	E_{S} [eV] ^{d)}	$E_{\text{S}}/E_{\text{T}}$ [eV] ^{e)}	ΔE_{ST} [eV] (exp./calc.) ^{f)}
1 (BuCzoB)	329, 409	481	89/20	47.2 (21)	28.7 (68)	-5.48/-2.45	3.03	2.87/2.79	0.082/0.17
2 (BuCzMeoB)	319, 401	468	92/20	42.0 (24)	26.2 (68)	-5.46/-2.40	3.06	2.90/2.81	0.095/0.21
3 (CzoB) ^{g)}	324, 387	463	79/19	38.3 (24)	71.6 (55)	-5.54/-2.46	3.08	2.95/2.80	0.15/0.27
4 (CzMeoB)	322, 381	453	69/19	32.2 (23)	83.7 (46)	-5.54/-2.42	3.12	2.99/2.85	0.15/0.28
5 (CzOMeoB)	320, 372	438	42/18	21.6 (14)	52.0 (28)	-5.54/-2.36	3.18	3.08/2.92	0.16/0.39

^{a)}In oxygen-free toluene at 298 K (2.0×10^{-5} M); ^{b)}Absolute photoluminescence quantum yields (PLQYs) in oxygen-free (N₂) and air-saturated (air) toluene at 298 K; ^{c)}PL lifetimes of prompt (τ_{p}) and delayed (τ_{d}) decay components for the oxygen-free toluene solutions at 298 K. The estimated prompt (Φ_{PF}) and delayed (Φ_{DF}) portions [%] in transient decay curves are given in parentheses; ^{d)}Estimated from the electrochemical oxidation (HOMO) and reduction (LUMO); ^{e)}Singlet (E_{S}) and triplet (E_{T}) energies estimated from onset wavelengths of the fluorescence and phosphorescence spectra obtained at 77 K; ^{f)} $\Delta E_{\text{ST}} = E_{\text{S}} - E_{\text{T}}$. Calculated ΔE_{ST} from TD-DFT at PBE0/6-31G(d,p). ^{g)}Data from Ref. ²¹.

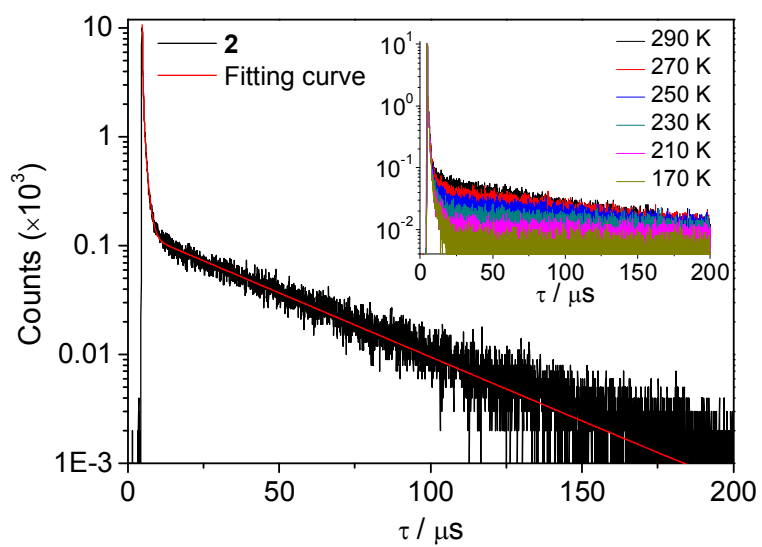


Figure 2.3. Transient PL decay curve of **2** in oxygen-free toluene at 298 K. The inset shows the temperature dependence of transient PL decay.

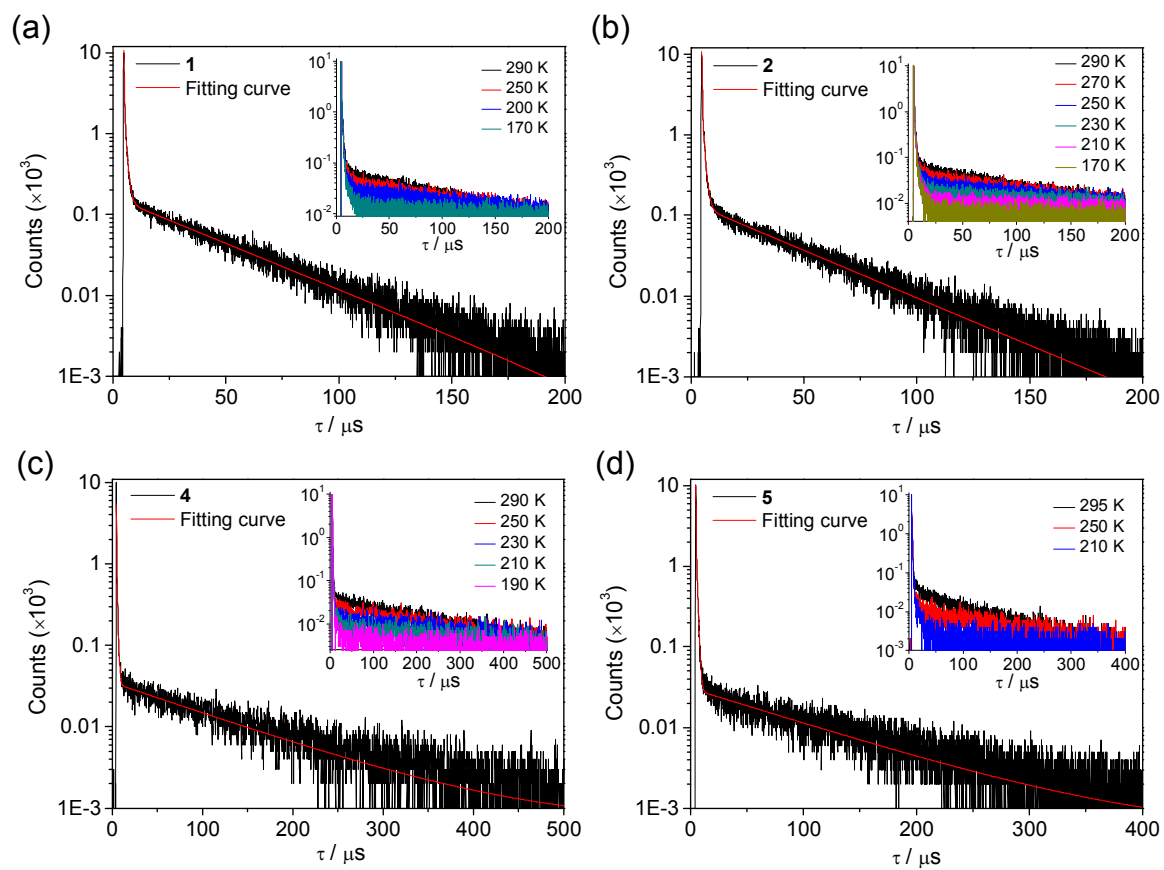


Figure 2.4. Transient PL decay curves of *ortho* D–A compounds in oxygen-free toluene at 298 K. Inset: temperature dependence of decay in oxygen-free toluene.

To gain insight into the geometric, electronic, and photophysical properties of the *ortho* D–A compounds, computational studies based on DFT were performed at the PBE0/6-31G(d,p) level (see Supporting Information for computational details). The geometries of ground (S_0) and excited (S_1 and T_1) states were fully optimized with the DFT and time-dependent DFT (TD-DFT) methods, respectively (Figure 2.5). The optimized dihedral angles between the Cz donor and acceptor moieties at the ground states are in a similar range (ca. 70–73°) for all compounds; this is comparable to that of the crystal structure of **2** (63.8°). The large dihedral angles indicate a twisted donor–acceptor structure, which is caused by the steric congestion in these *ortho* compounds. Accordingly, the HOMOs and LUMOs are locally distributed to the donor and acceptor moieties, respectively, leading to the effective spatial separation of the HOMO and LUMO. Note that the empty $p_\pi(B)$ orbital of the boron atom significantly contributes to the LUMO (Table 2.2). The extent of HOMO–LUMO separation was further determined by evaluating the overlap integral ($I_{H/L}$) between the wavefunctions for the HOMO and LUMO,^{5, 53} which is closely related to ΔE_{ST} (Figure 2.5 and Table 2.2). For all compounds, moderate $I_{H/L}$ values of ca. 24–27% are obtained with an increasing tendency from **1** to **5**.⁵⁴ As a result, the calculated ΔE_{ST} values are in the same order as the $I_{H/L}$ values ($\Delta E_{ST} = 0.17$ – 0.39 eV). Although these ΔE_{ST} values are slightly overestimated compared with the experimental values, the values follow the same qualitative order as that of the experimental ones (exp. ΔE_{ST} of **1** < **2** < **3** \approx **4** < **5**). In

particular, the order of the ΔE_{ST} values inversely matches with that of the delayed portion (Φ_{DF}) of PLQYs obtained from the transient decay curves, confirming that the contribution of delayed fluorescence depends on ΔE_{ST} , which governs the equilibration rate between the S_1 and T_1 states. Note that the lifetimes of delayed fluorescence (τ_d) of **1** and **2**, which possess small ΔE_{ST} values, are much shorter than those of **3–5** (Table 2.1). Therefore, based on the experimental and theoretical results, it can be deduced that *ortho* D–A compounds with electron-donating groups on the donor moiety (**1** and **2**) have small ΔE_{ST} values leading to strong delayed fluorescence and thereby high PLQY.^{31, 55-57} TD-DFT results also predict that the lowest-energy absorption and emission processes involve a HOMO–LUMO ICT transition (Table 2.3 and 2.4). The calculated transition energies are in good agreement with their experimental values, showing a gradual increase in energy following the order of **1** < **2** < **3** < **4** < **5**.

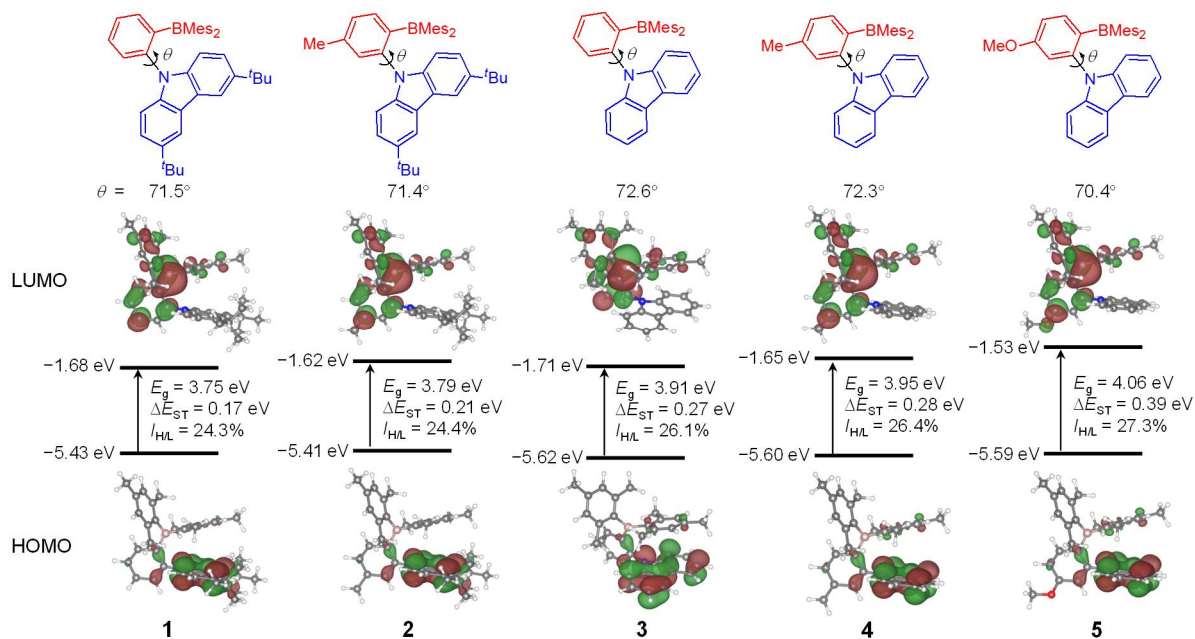


Figure 2.5. Optimized dihedral angles (θ , in degrees) between donor and phenylene (top) and frontier molecular orbitals, HOMO and LUMO, of 1–5 (isovalue = 0.03) at their ground state (S_0) geometries from DFT calculations (PCM in toluene). The orbital energies, HOMO–LUMO gaps (E_g), energy splitting between the S_1 and T_1 states (ΔE_{ST}), and overlap integral extents (I_{HL}) are presented.

Table 2.2. The contribution (in %) of donor and acceptor moieties to the frontier molecular orbitals and overlap integrals ($I_{H/L}$) between them for *ortho*-carbazole-appended triarylboron compounds (1–5).

	MO	energy (eV)	donor (3,6-(R ₁) ₂ -Cz)	acceptor (R ₂ -Ph)	acceptor (BMes ₂)	$I_{H/L}$
1 (BuCzoB)	LUMO	-1.68	2.14	35.22	62.63	24.3
	HOMO	-5.43	92.12	4.91	2.97	
2 (BuCzMeoB)	LUMO	-1.62	2.15	35.21	62.65	24.4
	HOMO	-5.41	91.96	4.98	3.07	
3 (CzoB)	LUMO	-1.71	2.12	34.26	63.61	26.1
	HOMO	-5.62	89.34	5.39	5.27	
4 (CzMeoB)	LUMO	-1.65	2.14	35.26	62.61	26.4
	HOMO	-5.60	89.20	5.35	5.46	
5 (CzOMeoB)	LUMO	-1.53	2.39	32.68	64.94	27.3
	HOMO	-5.59	88.49	5.60	5.91	

Table 2.3. The calculated absorption wavelength (λ_{abs} , in nm) and the corresponding oscillator strength (f) for *ortho*-carbazole-appended triarylboron compounds (1–5).

	λ_{abs}	f_{abs}
1 (BuCzoB)	428.0	0.0081
2 (BuCzMeoB)	421.7	0.0081
3 (CzoB)	408.4	0.0073
4 (CzMeoB)	402.7	0.0083
5 (CzOMeoB)	389.8	0.0119

Table 2.4. The calculated emission wavelength (λ_{abs} , in nm) and the corresponding oscillator strength (f) for *ortho*-carbazole-appended triarylboron compounds (1–5).

	λ_{em}	f_{em}
1 (BuCzoB)	503.8	0.0105
2 (BuCzMeoB)	491.9	0.0117
3 (CzoB)	477.8	0.0117
4 (CzMeoB)	467.4	0.0138
5 (CzOMeoB)	450.1	0.0138

III.2. Effect of the non-covalent interaction on the supramolecular formation

III.2.1. Molecular Borromean rings (BRs)

In the past two decades abiological self-assembly has emerged as a well-established method for the rational design of supramolecules by the independent pioneering work of Stang,⁵⁸ Fujita,⁵⁹ Raymond,⁶⁰ Mirkin,⁶¹ and others⁶² using the metal-ligand coordination. The coordination-driven self-assembly approach is now competing and complimenting the covalent synthetic methods for realizing the topologically complicated fascinating molecular architectures.⁶³ This approach is now being frequently used in the synthesis of commonly known threaded architectures such as catenanes, rotaxanes and links⁶⁴⁻⁶⁶. The synthesis of [2]catenanes has become routine⁶³ whereas the synthesis of more topologically complex, mechanically interlocked molecular architectures such as Borromean rings (BRs),⁶⁷ Solomon link,⁶⁸ star of David catenane⁶⁹ and pentafoil knots⁷⁰ is still a great challenge. Molecular BRs consists of three chemically independent rings that are locked in such a way that no two of the three rings are linked with each other as a Hopf link and opening of any one ring unlinks all.⁷¹ Recently the configuration of BRs was selected for the new logo of International Mathematical Union.⁷² BRs topology has been previously observed in DNA⁷³ and crystal packing,⁷⁴ and BRs intermediates⁷⁵ have also been reported. However, there are only two strategies known in the literature for the synthesis of discrete real (chemically non-connected) molecular BRs. Stoddart reported the first BRs associated with six Zn(II)

metal coordination,⁷⁶ subsequent demetallation provided real BRs along with free and open rings.⁷⁷ Jin reported another strategy using Cu(I) derived acceptor to produce real and associated BRs. However, the presence of paramagnetic Cu(I) nuclei restricted their NMR analysis to studying their purity and interconversion to monomeric rectangles (Figure 3.1).⁷⁸

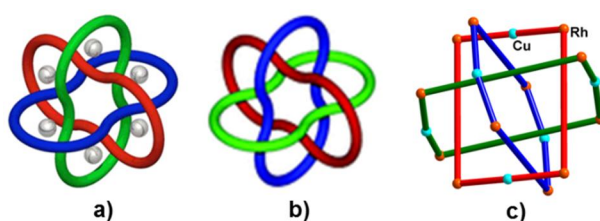
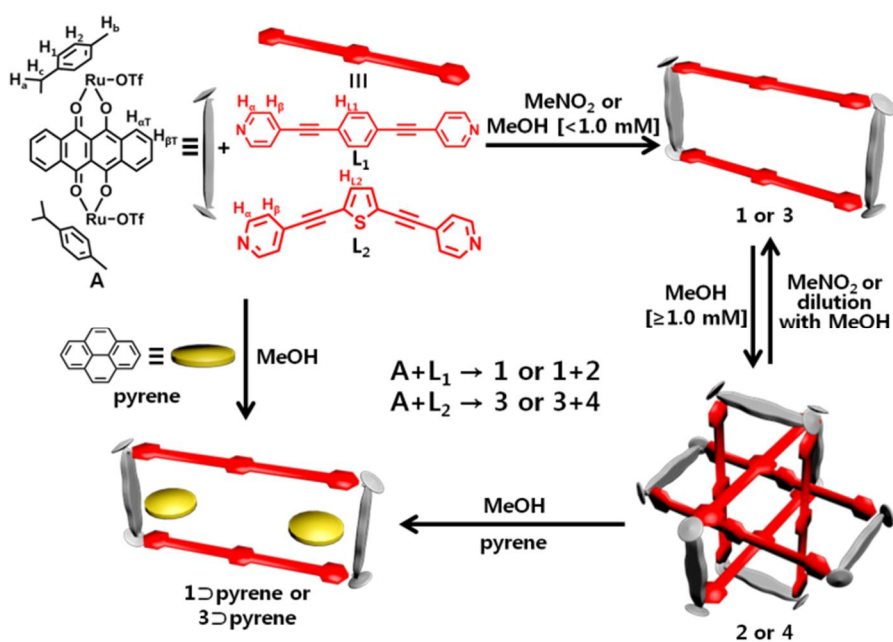


Figure 3.1. Reported examples of Borromean rings (a) Metal associated Borromean rings (b) Real Borromean rings after demetallation (c) Real Borromean rings wearing paramagnetic Cu(I) ions

With suitable modifications in the length, shape and functionality of the donor, we recently reported the template-free synthesis of a molecular Solomon link,^{79a} a Hopf's link,^{79b} an interlocked prismatic cage,^{79c} and a non-catenane “rectangle-in-rectangle”^{79d} through the combined strategy of coordination driven self-assembly and π - π stacking. Here we report the template-free self-assembly of BRs and solvent induced sequential interconversion of BRs to a monomeric ring by carefully selecting the dimensions and functionality of the donor and acceptor. The BRs topology was obtained from the

coordination-driven self-assembly of an arene-Ru(II) acceptor **A** and a ditopic ligand, 1,4-bis(4-pyridylethynyl) benzene (**L₁**) (Scheme 3.1).

Scheme 3.1. Self-assembly and interconversion of Borromean rings and monomeric rectangles.



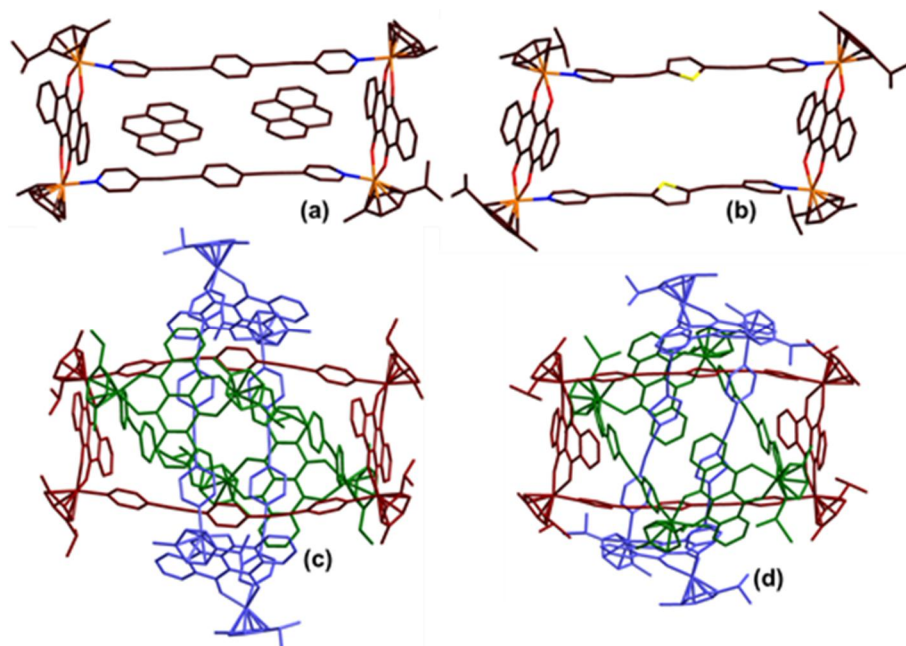


Figure 3.2. X-ray crystal structures of (a) $1 \supset (2 \cdot \text{pyrene})$, (b) **3**, (c) **2s** and (d) **4**. Hydrogen atoms and counter anions are omitted for clarity.

The single crystal X-ray diffraction (scXRD) analysis unambiguously confirmed the structures of **1** encapsulated with two molecules of pyrene, **3** (obtained from the CD_3NO_2 solution) and BRs **2** and **4** in the solid state (Figure 3.2). Considering the metallacycles as rectangles, the scXRD analysis confirmed the molecular structure of **2** with pyritohedral symmetry (T_h) wherein the three rings were found to be linked with the topology of BRs. Each of the three equivalent rings adopted a distorted rectangle like conformation with an average length and width (Ru-Ru distance) of 20.1 and 8.1 Å respectively. The three chemically non-connected distorted rectangles were held

together by CH $\cdots\pi$ (2.9 Å) interactions and multiple parallel-displaced π - π (3.5 Å) interactions between phenyl-ethynyl-pyridinyl moieties of the donor and tetracene moieties of the acceptor (Figure 3.3 and 3.4). The structure of **4** was also found similar to BRs **2** with average rectangular dimensions of 19.6 and 7.9 Å. In the structure of **1**, two pyrene molecules were found to be encapsulated and strongly interacted with the ethynyl-pyridinyl moiety stabilized via parallel-displaced π - π stacking (3.5 Å) and via CH $\cdots\pi$ (2.7 Å) interactions in edge-to-face fashion with the tetracene moiety of the acceptor. This observation clearly indicated that the driving forces in the formation of BRs are multiple π - π and CH $\cdots\pi$ interactions, which is also supported by the theoretically obtained spatial distribution of noncovalent interaction (NCI) by plotting the iso-surfaces of reduced density gradient (RDG) as shown in Figure 3.5.⁸⁰

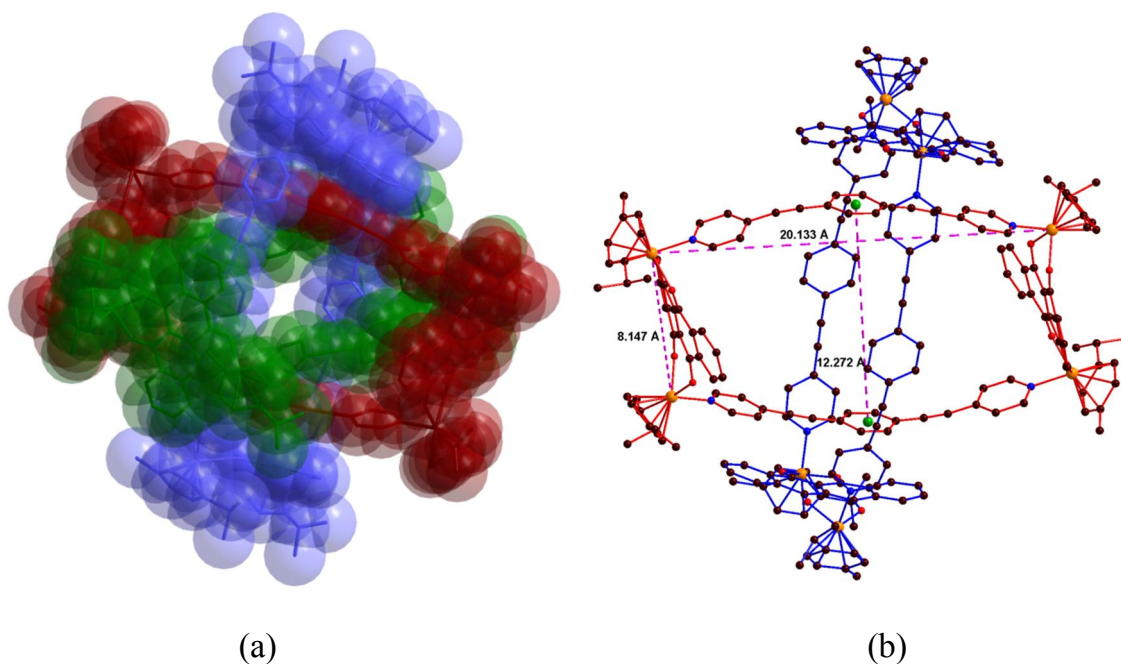


Figure 3.3. Crystal structure of Borromean rings **2** (a) in space filling model (b) Length and breadth of the ring in Borromean rings topology (one of the rings has been deleted for clarity)

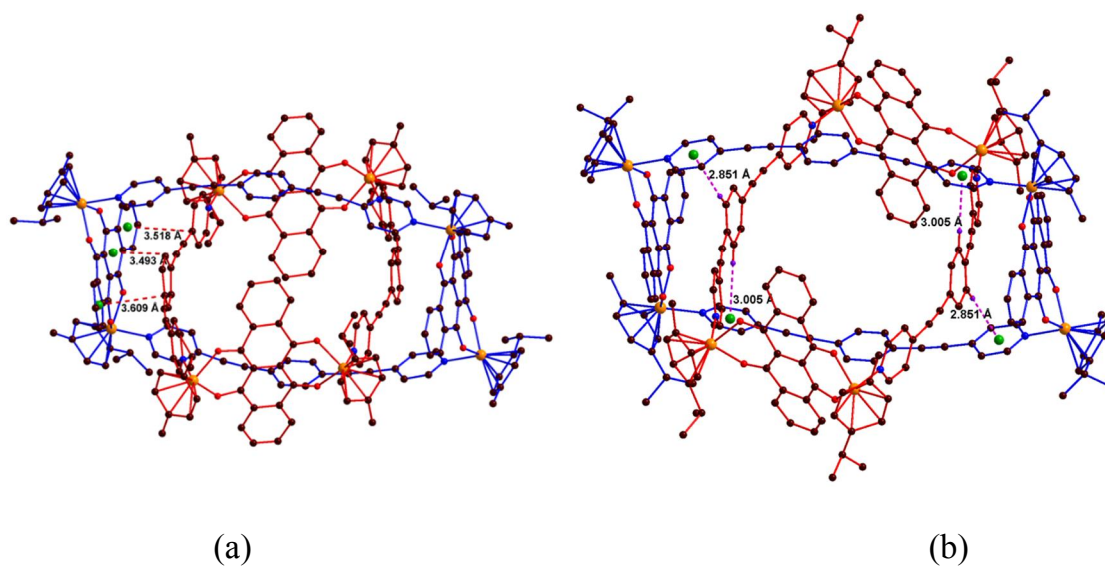


Figure 3.4. Crystal structure of Borromean rings **2** in ball-stick model showing (a) $\pi \cdots \pi$ and (b) $\text{CH} \cdots \pi$ interactions responsible for Borromean rings topology (one of the rings has been deleted for clarity)

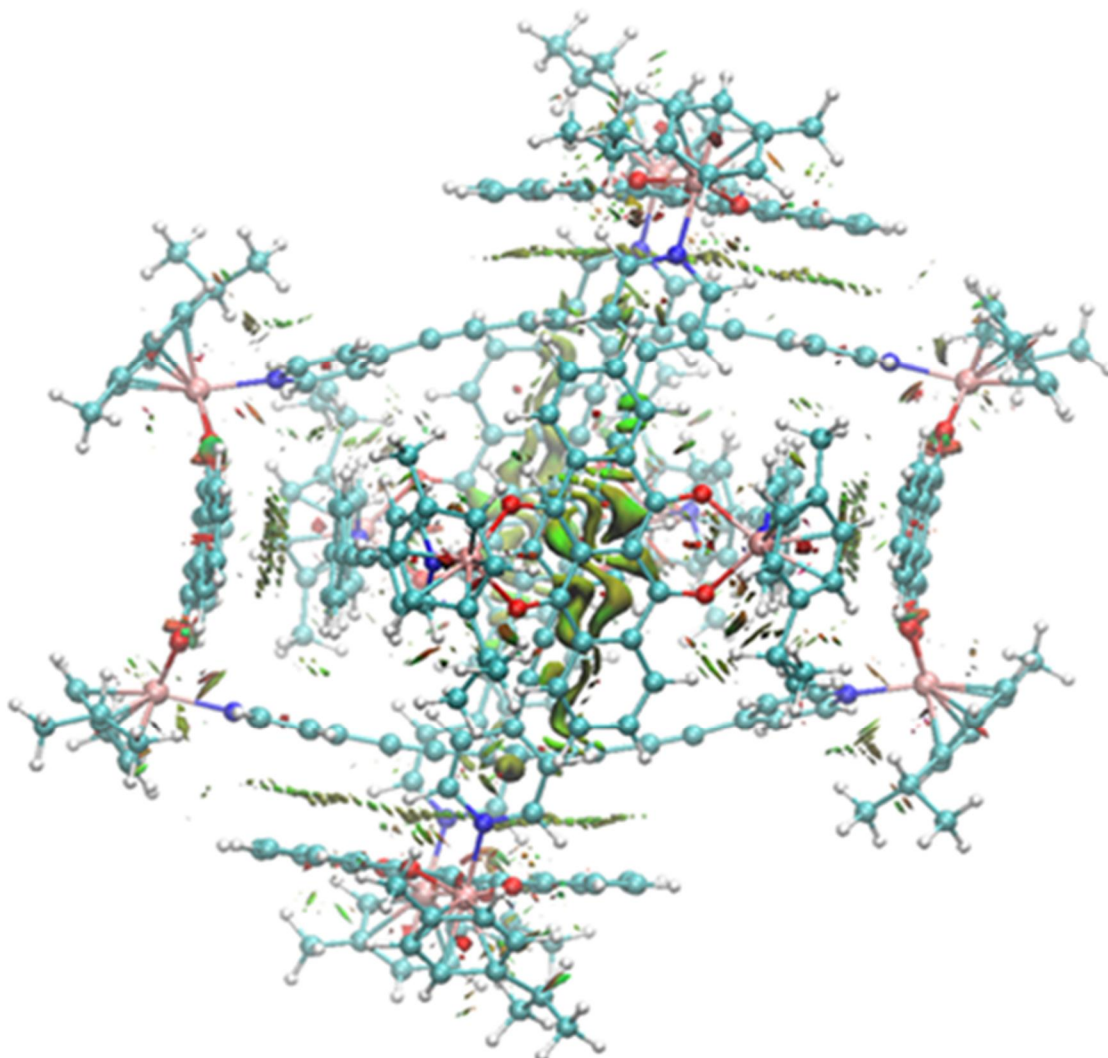


Figure 3.5. RDG iso-surfaces ($s = 0.5$ au) for BRs **2**. The surfaces are colored on a blue–green–red scale according to the values of $\text{sign}(\lambda_2)\rho$, ranging from -0.02 to $+0.02$ au. The primary intermolecular interactions are the π - π interactions between phenyl- ethynyl-pyridinyl moieties of donor **L**₁ and tetracene moieties of the acceptor **A**, which are indicated by green iso-surfaces.

To shed light on the formation of Borromean rings (BRs) **2**, we carried out the computational study using DFT methods implemented in Gaussian09 software package.⁸¹ Due to the huge size of supramolecular compound, we employed the geometry of BRs **2** determined by means of X-ray diffraction (XRD) experiment. Therefore, the positions of only hydrogen atoms were optimized and other atoms were fixed at the positions observed by XRD in the ω B97X-D/3-21G level of theory at the gas phase.⁸² The binding energy (BE) was evaluated using three different hybrid functionals, ω B97X-D,⁸² M06-2X,⁸³ and PBE0,⁸⁴ and 6-31G basis set with the geometry obtained by the above-mentioned process. For Ru atoms, LanL2DZ effective pseudo-potential and corresponding basis set were used for all the calculations.⁸⁵ Whereas PBE0 cannot describe vdW interaction, both ω B97X-D and M06-2X were designed to effectively deal with the weakly interacting systems. The charge states of +12 and +4 were assigned for BRs and MRs, respectively, on which we did not find the instability, i.e., valence electrons at unbound state, due to such large charge states in the electronic structures obtained from DFT calculations. During the single-point calculations for evaluating BE ($BE = E(\text{BRs}) - \{E(\text{MR1}) + E(\text{MR2}) + E(\text{MR3})\}$, MR: monomeric ring), the polarizable continuum model (PCM) using the integral equation formalism variant (IEFPCM) was employed to consider the influence of solvent, i.e., methanol, medium.⁸⁶ The formation of BRs **2**, leads to the reduction of the solvent accessible surface area by $\sim 172 \text{ \AA}^2$. The experimentally observed increase of BRs synthesis yield due to the addition of more polar solvent (D_2O) into CD_3OD medium

can be explained by that the interlocking supramolecular process reduces the contacts between solvent molecules and the hydrophobic parts, i.e., ethynyl-phenyl moieties, and thus overall process can proceed more spontaneously in more highly polar medium. The evaluated BEs are -127.8 , -58.9 , and $+26.6$ kcal/mol for ω B97X-D, M06-2X, and PBE0 methods, respectively. The results obtained by ω B97X-D methods of -127.8 kcal/mol can be examined with the contribution of long-range dispersive intermolecular interaction. The lower binding energy obtained with M06-2X relative to that from ω B97X-D can be understood by the poor performance of M06-2X out of equilibrium position,⁸⁷ although both M06-2X and ω B97X-D were designed to effectively deal with the noncovalent interaction (NCI). The endothermic BE with PBE0 also implies that the NCI plays a crucial role in the formation of BRs because of the lack of PBE0 in describing it. We further examined the spatial distribution of NCI by plotting the iso-surface of reduced density gradient (RDG, $s = 1/(2(3\pi^2)^{1/3}|\nabla\rho|/\rho^{4/3})$, for which MULTIWFN program was utilized (Figure 3.5).⁸⁸ The RDG plot is helpful to spatially investigate a deviation from a homogeneous electron distribution during supramolecular assembly.⁸⁹ Figure 3.5 clearly unveiled that NCI in BRs **2** is mainly described by the π - π interactions between phenyl-ethynyl-pyridinyl moieties of donor **L**₁ and tetracene moieties of the acceptor **A**.

IV. Conclusion

In this paper, two major topics are covered. For the first study on TADF, first we designed ortho- and para-D-A molecules using DPA, PXZ and Cz donors and BMe₂ acceptors, and examined their TADF properties include the geometric, electronic, and photophysical properties. In particular, interesting results that ortho- and para-D-A compounds using DPA and Cz donors have the same donor and acceptor, ortho-D-A compounds have small enough ΔE_{ST} for TADF, while the para-D-A compounds show more larger (0.20 and 0.15 eV for DPAoB and CzoB, respectively). Secondly, in the color tuning study based on CzoB molecule, it was confirmed that the LUMO level can be effectively controlled by substituting the methyl group and methoxy group in the phenylene spacer, and also, it can be controlled the HOMO level using Cz and BuCz donor. Accordingly, we found that not only the species of donor and acceptor but also the geometry of molecules is very important point in designing TADF molecules. In addition, a successful color tuning study could be performed with a strategic design on the donor and acceptor.

The second topic covered the factors contributing to the formation and stabilization of supramolecules in the two systems. To understand this, we focused on the structural features of supramolecules and we obtained convincing results by calculating the binding energy of molecules using several DFT hybrid functionals. The results obtained

by ω B97X-D and M06-2X methods can be examined with the contribution of long-range dispersive intermolecular interaction. The endothermic binding energy with PBE0 also implies that the NCI plays a crucial role in the formation of supramolecules because of the lack of PBE0 in describing it.

V. Reference

1. Pope, M.; Kallmann, H. P.; Magnante, P. Electroluminescence in Organic Crystals. *J. Chem. Phys.* **1963**, *38*, 2042–2043.
2. M. Y. Wong, E. Zysman-Colman, *Adv. Mater.* **2017**, *29*, 1605444.
3. Y. Im, M. Kim, Y. J. Cho, J.-A. Seo, K. S. Yook, J. Y. Lee, *Chem. Mater.* **2017**, *29*, 1946-1963.
4. Z. Yang, Z. Mao, Z. Xie, Y. Zhang, S. Liu, J. Zhao, J. Xu, Z. Chi, M. P. Aldred, *Chem. Soc. Rev.* **2017**, *46*, 915-1016.
5. Y. Tao, K. Yuan, T. Chen, P. Xu, H. Li, R. Chen, C. Zheng, L. Zhang, W. Huang, *Adv. Mater.* **2014**, *26*, 7931-7958.
6. C. Adachi, *Jpn. J. Appl. Phys.* **2014**, *53*, 060101.
7. Q. Zhang, J. Li, K. Shizu, S. Huang, S. Hirata, H. Miyazaki, C. Adachi, *J. Am. Chem. Soc.* **2012**, *134*, 14706-14709.
8. K. Goushi, K. Yoshida, K. Sato, C. Adachi, *Nat. Photonics* **2012**, *6*, 253-258.
9. H. Uoyama, K. Goushi, K. Shizu, H. Nomura, C. Adachi, *Nature* **2012**, *492*, 234-238.
10. H. Kaji, H. Suzuki, T. Fukushima, K. Shizu, K. Suzuki, S. Kubo, T. Komino, H. Oiwa, F. Suzuki, A. Wakamiya, Y. Murata, C. Adachi, *Nat. Commun.* **2015**, *6*, 8476.
11. S. Hirata, Y. Sakai, K. Masui, H. Tanaka, S. Y. Lee, H. Nomura, N. Nakamura, M. Yasumatsu, H. Nakanotani, Q. Zhang, K. Shizu, H. Miyazaki, C. Adachi, *Nat. Mater.* **2015**, *14*, 330-336.

12. Q. Zhang, H. Kuwabara, W. J. Potscavage, Jr., S. Huang, Y. Hatae, T. Shibata, C. Adachi, *J. Am. Chem. Soc.* **2014**, *136*, 18070-18081.
13. J. W. Sun, J. H. Lee, C. K. Moon, K. H. Kim, H. Shin, J.-J. Kim, *Adv. Mater.* **2014**, *26*, 5684-5688.
14. Q. Zhang, B. Li, S. Huang, H. Nomura, H. Tanaka, C. Adachi, *Nat. Photonics* **2014**, *8*, 326-332.
15. F. B. Dias, K. N. Bourdakos, V. Jankus, K. C. Moss, K. T. Kamtekar, V. Bhalla, J. Santos, M. R. Bryce, A. P. Monkman, *Adv. Mater.* **2013**, *25*, 3707-3714.
16. J. Li, T. Nakagawa, J. MacDonald, Q. Zhang, H. Nomura, H. Miyazaki, C. Adachi, *Adv. Mater.* **2013**, *25*, 3319-3323.
17. W. Hohenberg, P.; Kohn., *Phys. Rev.*, **1964**, *136*, 864-871.
18. Lee, June-Gunn, *Computational science for materials*, Young publications, **2014**, 144-153.
19. W. Koch, M. C. Holthausen, *A Chemist's Guide to Density Functional Theory*, Wiley-vch, **2015**, 33-43
20. Marques, M.A.L., Ullrich, C., Nogueira, F., Rubio, A., Burke, K., Gross, E.K.U., *Time-Dependent Density Functional Theory*, Springer, **2006**, 1-23
21. L. Bergmann, D. M. Zink, S. Bräse, T. Baumann and D. Volz, *Top. Curr. Chem.*, **2016**, *374*, 1-39.
22. Y. Kitamoto, T. Namikawa, T. Suzuki, Y. Miyata, H. Kita, T. Sato, S. Oi, *Org. Electron.* **2016**, *34*, 208-217.

23. K. Suzuki, S. Kubo, K. Shizu, T. Fukushima, A. Wakamiya, Y. Murata, C. Adachi, H. Kaji, *Angew. Chem. Int. Ed.* **2015**, *54*, 15231-15235.
24. Tao, Y.; Yuan, K.; Chen, T.; Xu, P.; Li, H.; Chen, R.; Zheng, C.; Zhang, L.; Huang, W. Thermally Activated Delayed Fluorescence Materials Towards the Breakthrough of Organoelectronics. *Adv. Mater.* **2014**, *26*, 7931-7958.
25. Endo, A.; Ogasawara, M.; Takahashi, A.; Yokoyama, D.; Kato, Y.; Adachi, C. Thermally Activated Delayed Fluorescence from Sn⁴⁺-Porphyrin Complexes and Their Application to Organic Light Emitting Diodes — A Novel Mechanism for Electroluminescence. *Adv. Mater.* **2009**, *21*, 4802-4806.
26. Chen, T.; Zheng, L.; Yuan, J.; An, Z.; Chen, R.; Tao, Y.; Li, H.; Xie, X.; Huang, W. Understanding the Control of Singlet-Triplet Splitting for Organic Exciton Manipulating: A Combined Theoretical and Experimental Approach. *Sci. Rep.* **2015**, *5*, 10923.
27. Y. H. Lee, S. Park, J. Oh, J. W. Shin, J. Jung, S. Yoo, M. H. Lee, *ACS Appl. Mater. Interfaces* **2017**, *9*, 24035-24042.
28. D. R. Lee, J. M. Choi, C. W. Lee, J. Y. Lee, *ACS Appl. Mater. Interfaces* **2016**, *8*, 23190-23196.
29. P. Rajamalli, N. Senthilkumar, P. Gandeepan, P. Y. Huang, M. J. Huang, C. Z. Ren-Wu, C. Y. Yang, M. J. Chiu, L. K. Chu, H. W. Lin, C. H. Cheng, *J. Am. Chem. Soc.* **2016**, *138*, 628-634.
30. J.-R. Cha, C. W. Lee, J. Y. Lee, M.-S. Gong, *Dyes Pigm.* **2016**, *134*, 562-568.
31. Y. Liu, G. Xie, K. Wu, Z. Luo, T. Zhou, X. Zeng, J. Yu, S. Gong, C. Yang, *J. Mater. Chem. C* **2016**, *4*, 4402-4407.
32. Y. Kitamoto, T. Namikawa, T. Suzuki, Y. Miyata, H. Kita, T. Sato, S. Oi, *Org. Electron.* **2016**, *34*, 208-217.

33. Y. Kitamoto, T. Namikawa, D. Ikemizu, Y. Miyata, T. Suzuki, H. Kita, T. Sato, S. Oi, *J. Mater. Chem. C* **2015**, *3*, 9122-9130.
34. K. Suzuki, S. Kubo, K. Shizu, T. Fukushima, A. Wakamiya, Y. Murata, C. Adachi, H. Kaji, *Angew. Chem. Int. Ed.* **2015**, *54*, 15231-15235.
35. M. Numata, T. Yasuda, C. Adachi, *Chem. Commun.* **2015**, *51*, 9443-9446.
36. K. Matsui, S. Oda, K. Yoshiura, K. Nakajima, N. Yasuda, T. Hatakeyama, *J. Am. Chem. Soc.* **2018**, *140*, 1195-1198.
37. T. Hatakeyama, K. Shiren, K. Nakajima, S. Nomura, S. Nakatsuka, K. Kinoshita, J. Ni, Y. Ono, T. Ikuta, *Adv. Mater.* **2016**, *28*, 2777-2781.
38. H. Hirai, K. Nakajima, S. Nakatsuka, K. Shiren, J. Ni, S. Nomura, T. Ikuta, T. Hatakeyama, *Angew. Chem. Int. Ed.* **2015**, *54*, 13581-13585.
39. C. Y. Chan, L. S. Cui, J. U. Kim, H. Nakanotani, C. Adachi, *Adv. Funct. Mater.* **2018**, *28*, 1706023.
40. Y. Wada, S. Kubo, H. Kaji, *Adv. Mater.* **2018**, *30*, 1705641.
41. Q. Liang, C. Han, C. Duan, H. Xu, *Adv. Opt. Mater.* **2018**, *6*, 1800020.
42. Y. Li, J.-Y. Liu, Y.-D. Zhao, Y.-C. Cao, *Mater. Today* **2017**, *20*, 258-266.
43. Y. Im, S. Y. Byun, J. H. Kim, D. R. Lee, C. S. Oh, K. S. Yook, J. Y. Lee, *Adv. Funct. Mater.* **2017**, *27*, 1603007.
44. M. Godumala, S. Choi, M. J. Cho, D. H. Choi, *J. Mater. Chem. C* **2016**, *4*, 11355-11381.
45. M. Kim, S. K. Jeon, S. H. Hwang, J. Y. Lee, *Adv. Mater.* **2015**, *27*, 2515-2520.

46. P. Rajamalli, N. Senthilkumar, P.-Y. Huang, C.-C. Ren-Wu, H.-W. Lin, C.-H. Cheng, *J. Am. Chem. Soc.* **2017**, *139*, 10948-10951.
47. P. Rajamalli, V. Thangaraji, N. Senthilkumar, C.-C. Ren-Wu, H.-W. Lin, C.-H. Cheng, *J. Mater. Chem. C* **2017**, *5*, 2919-2926.
48. L. M. Lifshits, D. S. Budkina, V. Singh, S. M. Matveev, A. N. Tarnovsky, J. K. Klosterman, *Phys. Chem. Chem. Phys.* **2016**, *18*, 27671-27683.
49. L. Mei, J. Hu, X. Cao, F. Wang, C. Zheng, Y. Tao, X. Zhang, W. Huang, *Chem. Commun.* **2015**, *51*, 13024-13027.
50. F. Jäkle, *Chem. Rev.* **2010**, *110*, 3985-4022.
51. T. W. Hudnall, C.-W. Chiu, F. P. Gabbaï, *Acc. Chem. Res.* **2009**, *42*, 388-397.
52. Z. M. Hudson, S. Wang, *Acc. Chem. Res.* **2009**, *42*, 1584-1596.
53. Endo, M. Ogasawara, A. Takahashi, D. Yokoyama, Y. Kato, C. Adachi, *Adv. Mater.* **2009**, *21*, 4802-4806.
54. T. Chen, L. Zheng, J. Yuan, Z. An, R. Chen, Y. Tao, H. Li, X. Xie, W. Huang, *Sci. Rep.* **2015**, *5*, 10923.
55. D. Zhang, M. Cai, Y. Zhang, D. Zhang, L. Duan, *Mater. Horiz.* **2016**, *3*, 145-151.
56. C. Duan, J. Li, C. Han, D. Ding, H. Yang, Y. Wei, H. Xu, *Chem. Mater.* **2016**, *28*, 5667-5679.
57. Y. J. Cho, K. S. Yook, J. Y. Lee, *Adv. Mater.* **2014**, *26*, 6642-6646.
58. (a) Leininger, S.; Olenyuk, B.; Stang, P. J. *Chem. Rev.* **2000**, *100*, 853. (b) Seidel, S.R.; Stang, P.J. *Acc. Chem. Res.*, **2002**, *35*, 972. (c) Northrop, B. H.; Zheng, Y.-R.; Chi, K.-W.; Stang, P. J. *Acc. Chem. Res.* **2009** *42*, 1554. (d) Chakrabarty, R.; Mukherjee, P. S.; Stang, P.

J. Chem. Rev. **2011**, *111*, 6810. (e) Cook, T. R.; Vajpayee, V.; Lee, M. H.; Stang, P. J.; Chi, K.-W. *Acc. Chem. Res.* **2013**, *46*, 2464. (f) Cook, T. R.; Stang, P. J. *Chem. Rev.* **2015**, *115*, 7001.

59. (a) Fujita, M.; *Chem. Soc. Rev.* **1998**, *27*, 417. (b) Fujita, M.; Tominaga, M.; Hori, A.; Therrien, B. *Acc. Chem. Res.* **2005**, *38*, 369. (c) Yoshizawa, M.; Klosterman, J. K.; Fujita, M. *Angew. Chem., Int. Ed.* **2009**, *48*, 3418.

60. (a) Pluth, M. D.; Raymond, K. N. *Chem. Soc. Rev.* **2007**, *36*, 161. (b) Caulder, D. L.; Raymond, K. N. *Acc. Chem. Res.* **1999**, *32*, 975.

61. (a) Gianneschi, N. C.; Masar, M. S., III; Mirkin, C. A. *Acc. Chem. Res.* **2005**, *38*, 825 (b) Holliday, B. J.; Mirkin, C. A. *Angew. Chem., Int. Ed.* **2001**, *40*, 2022.

62. (a) McConnell, A. J., Wood, C. S., Neelakandan, P. P.; Nitschke, J. R. *Chemical Reviews* **2015**, *115*, 7729. (b) Zarra, S.; Wood, D. M.; Roberts, D. A.; Nitschke, J. R. *Chem. Soc. Rev.* **2015**, *44*, 419. (c) Han, Y. F.; Jin, G. X. *Chem. Soc. Rev.* **2014**, *43*, 2799. (d) Han, Y.-F.; Jin, G.-X. *Acc. Chem. Res.* **2014**, *47*, 3571. (e) Mukherjee, S.; Mukherjee, P. S. *Chem. Commun.* **2014**, *50*, 2239. (f) Singh, N.; Jo, J.-H.; Song, Y. H.; Kim, H.; Kim, D.; Lah, M. S.; Chi, K.-W. *Chem. Commun.* **2015**, *51*, 4492. (g) Dolomanov, O. V.; Blake, A. J.; Champness, N. R.; Schröder, M.; Wilson, C. *Chem. Commun.* **2003**, 682.

63. (a) Forgan, R. S.; Sauvage, J.-P.; Stoddart, J. F. *Chem. Rev.* **2011**, *111*, 5434. (b) Gil-Ramirez, G.; Leigh, D. A.; Stephens, A. J. *Angew. Chem., Int. Ed.* **2015**, *54*, 6110. (c) De, S.; Mahata, K.; Schmittel, M. *Chem. Soc. Rev.* **2010**, *39*, 1555.

64. (a) Sauvage, J.-P.; Dietrich-Buchecker, C., Eds. *Molecular Catenanes, Rotaxanes, and Knots: A Journey Through the World of Molecular Topology*; Wiley-VCH: Weinheim, Germany, **1999**. (B) Fujita, M. *Acc. Chem. Res.* **1999**, *32*, 53.

65. (a) Wood, C. S.; Ronson, T. K.; Belenguer, A. M.; Holstein, J. J.; Nitschke, J. R. *Nat. Chem.* **2015**, *7*, 354. (b) Kottas, G. S.; Clarke, L. I.; Horinek, D.; Michl, J. *Chem. Rev.* **2005**,

105, 1281.

66. Beves, J. E.; Blight, B. A.; Campbell, C. J.; Leigh, D. A.; McBurney, R. T. *Angew. Chem., Int. Ed.* **2011**, *50*, 9260.

67. (a) Cantrill, S. J.; Chichak, K. S.; Peters, A. J.; Stoddart, J. F. *Acc. Chem. Res.* **2005**, *38*, 1. (b) Meyer, C. D.; Forgan, R. S.; Chichak, K. S.; Peters, A. J.; Tangchaivang, N.; Cave, G. W. V.; Khan, S. I.; Cantrill, S. J.; Stoddart, J. F. *Chem.-Eur. J.* **2010**, *16*, 12570.

68. (a) F. Ibukuro, M. Fujita, K. Yamaguchi, J.-P. Sauvage, *J. Am. Chem. Soc.* **1999**, *121*, 11014. (b) Beves, J. E.; Danon, J. J.; Leigh, D. A.; Lemonnier, J.-F.; Vitorica-Yrezabal, I. *J. Angew. Chem. Int. Ed.* **2015**, *54*, 7555. (c) Ponnuswamy, N.; Cougnon, F. B. L.; Pantoş, D. G.; Sanders, J. K. M. *J. Am. Chem. Soc.* **2014**, *136*, 8243. (d) Prakasam, T.; Lusi, M.; Elhabiri, M.; Platas-Iglesias, C.; Olsen, J. C.; Asfari, Z.; Cianfèrani-Sanglier, S.; Debaene, F.; Charbonnière, L. J.; Trabolsi, A. *Angew. Chem., Int. Ed.* **2013**, *52*, 9956.

69. Leigh, D. A.; Pritchard, R. G.; Stephens, A. J. *Nat. Chem.* **2014**, *6*, 978.

70. (a) Ayme, J.-F.; Beves, J. E.; Leigh, D. A.; McBurney, R. T.; Rissanen, K.; Schultz, D. *Nat. Chem.* **2012**, *4*, 15. (b) Ayme, J.-F.; Beves, J. E.; Leigh, D. A.; McBurney, R. T.; Rissanen, K.; Schultz, D. *J. Am. Chem. Soc.* **2012**, *134*, 9488.

71. C.C. Adams, *The knot book: an elementary introduction to the mathematical theory of knots.* *American Mathematical Soc.* **2004**.

72. Gunn, C.; Sullivan, J. M. *The Borromean Rings: A video about the new IMU logo.* *Bridges Proceedings (Leeuwarden)*, **2008**, 63.

73. Mao, C.; Sun, W.; Seeman, N. C. *Nature* **1997**, *386*, 137.

74. Thorp-Greenwood, F. L.; Kulak, A. N.; Hardie, M. J. *Nat. Chem.* **2015**, *7*, 526. (b) Liantonio, R.; Metrangolo, P.; Meyer, F.; Pilati, T.; Navarrini, W.; Resnatti, G. *Chem. Commun.* **2006**, 1819.

75. (a) Loren, J. C.; Yoshizawa, M.; Haldimann, R. F.; Linden, A.; Siegel, J. S. *Angew. Chem., Int. Ed.* **2003**, *42*, 5702. (b) Schalley, C. A. *Angew. Chem., Int. Ed.* **2004**, *43*, 4399.

76. (a) Chichak, K. S.; Cantrill, S. J.; Pease, A. R.; Chiu, S. H.; Cave, G. W. V.; Atwood, J. L.; Stoddart, J. F. *Science* **2004**, *304*, 1308. (b) Chichak, K. S.; Peters, A. J.; Cantrill, S. J.; Stoddart, J. F. *J. Org. Chem.* **2005**, *70*, 7956.

77. Peters, A. J.; Chichak, K. S.; Cantrill, S. J.; Stoddart, J. F. *Chem. Commun.* **2005**, 3394.

78. (a) Huang, S-L.; Lin, Y-J.; Andy Hor, T. S.; Jin, G-X. *J. Am. Chem. Soc.* **2013**, *135*, 8125. (b) Huang, S-L.; Lin, Y-L.; Li, Z-H.; Jin, G-X. *Angew. Chem. Int. Ed.* **2014**, *53*, 11218.

79. (a) Song, Y. H.; Singh, N.; Jung, J.; Kim, H.; Kim, E.-H.; Cheong, H.-K.; Kim, Y.; Chi, K.-W. *Angew. Chem. Int. Ed.* **2016**, *55*, 2007. (b) Lee, H.; Elumalai, P.; Singh, N.; Kim, H.; Lee, S. U.; Chi, K.-W. *J. Am. Chem. Soc.* **2015**, *137*, 4674. (c) Mishra, A.; Dubey, A.; Min, J. W.; Kim, H.; Stang, P. J.; Chi, K.-W. *Chem. Commun.* **2014**, *50*, 7542. (d) Vajpayee, V.; Song, Y. H.; Cook, T. R.; Kim, H.; Lee, Y.; Stang, P. J.; Chi, K.-W. *J. Am. Chem. Soc.* **2011**, *133*, 19646.

80. Density functional theory computations were performed to study the intermolecular interactions in BRs **2**. The binding energies (BE) evaluated using three different hybrid functionals were -127.8 (ω B97X-D), -58.9 (M06-2X), and $+26.6$ kcal/mol (PBE0), with the geometry determined by scXRD. The variation of BE of employed methods, according to their performance in describing NCI, clearly indicates that the NCI plays a crucial role in the formation of BRs.

81. Frisch, M. J.; Trucks, G. W.; Schlegel, H. B.; Scuseria, G. E.; Robb, M. A.; Cheeseman, J. R.; Scalmani, G.; Barone, V.; Mennucci, B.; Petersson, G. A.; Nakatsuji, H.; Caricato, M.; Li, X.; Hratchian, H. P.; Izmaylov, A. F.; Bloino, J.; Zheng, G.; Sonnenberg, J. L.; Hada, M.; Ehara, M.; Toyota, K.; Fukuda, R.; Hasegawa, J.; Ishida, M.; Nakajima, T.; Honda, Y.; Kitao, O.; Nakai, H.; Vreven, T.; Montgomery, J. A., Jr.; Peralta, J. E.; Ogliaro, F.; Bearpark, M.; Heyd, J. J.; Brothers, E.; Kudin, K. N.; Staroverov, V. N.; Kobayashi, R.; Normand, J.;

Raghavachari, K.; Rendell, A.; Burant, J. C.; Iyengar, S. S.; Tomasi, J.; Cossi, M.; Rega, N.; Millam, J. M.; Klene, M.; Knox, J. E.; Cross, J. B.; Bakken, V.; Adamo, C.; Jaramillo, J.; Gomperts, R.; Stratmann, R. E.; Yazyev, O.; Austin, A. J.; Cammi, R.; Pomelli, C.; Ochterski, J. W.; Martin, R. L.; Morokuma, K.; Zakrzewski, V. G.; Voth, G. A.; Salvador, P.; Dannenberg, J. J.; Dapprich, S.; Daniels, A. D.; Farkas, Ö.; Foresman, J. B.; Ortiz, J. V.; Cioslowski, J.; Fox, D. J. Gaussian 09, Revision E.01, Gaussian, Inc., Wallingford CT, 2009, <http://www.gaussian.com>.

82. Chai, J. D.; Head-Gordon M. *Phys. Chem. Chem. Phys.* **2008**, *10*, 6615.

83. Hay, P. J.; Wadt, W. R. *J. Chem. Phys.* **1985**, *82*, 299.

84. Zhao, Y.; Truhlar D. G. *Theor. Chem. Acc.* **2008**, *120*, 215.

85. Adamo, C.; Barone, V. *J. Chem. Phys.* **1999**, *110*, 6158.

86. Scalmani, G.; Frisch, M. J. *J. Chem. Phys.* **2010**, *132*, 114110.

87. Vydrov, O. A.; Van Voorhis, T. *J. Chem. Theory Comput.* **2012**, *8*, 1929.

88. Lu, T.; Chen, F. *J. Comput. Chem.* **2012**, *33*, 580.

89. Johnson, E. R.; Keinan, S.; Mori-Sánchez, P.; Contreras-García, J.; Cohen, A. J.; Yang, W. *J. Am. Chem. Soc.* **2010**, *132*, 6498.